Investigating Wave Loads and Energy of a Spherical Object Using Numerical and Experimental Methods

Erling Calvert Dolve

Master's thesis in Ocean Technology

University of Bergen

Department of Physics and Technology

November 2023

Acknowledgements

While this thesis is the result of my multiple years of studies, it would not be possible without the support of several people.

First of all, I want to thank my supervisors Associate Professor Saeed Bikass, Associate Professor Mariusz Domagala, Associate Professor Hassan Momeni, and Professor Bjørn Tore Hjertaker. Without your guidance, suggestions, input, and help, I would have been lost on numerous occasions. Your enthusiasm and knowledge has inspired me.

I want to thank the laboratory engineers at MarinLab for guiding me through the experimental part of the thesis. An extra thanks to Engineer Torstein Frantzen and Associate Professor Gloria Maria Stenfelt, who helped me with mounting solutions, controlling the equipment, and giving input on tweaks to improve the accuracy of the measurements. Thank you to Engineer Harald Moen as well for helping me manufacture parts from my drawings and to the rest of the engineering department connected to MarinLab. Also, thank you to Student Councelor Irlin Nyland for answering any questions and helping out with other academic problems.

Lastly, I would like to thank my fellow students from the University of Bergen, my friends and family, and my partner Carina. Thank you for sharing your knowledge, good times, and tough times. I would not have changed anything about our time as students together.

Abstract

The world is undergoing massive changes due to climate change. To combat this, renewable energy sources are required. Whereas solar, wind, and hydropower are viable alternatives, wave power offers more stability and is a largely untapped energy source. This thesis aims to contribute to further research on optimizing wave energy converters by analyzing the available energy in waves, wave loads, energy corresponding to the wave loads, and the percentage of available energy that can be harvested. This has been done using Computational Fluid Dynamics (CFD) and experimental testing in MarinLab, the hydrodynamic test facility at Western Norway University of Applied Sciences (HVL). A sphere with a diameter of 200 mm was used, and the loads in the horizontal drag direction and vertical lift direction onto the sphere were measured using two load cells. From CFD, the drag and lift forces, drag and lift coefficients, and the wet surface area projected by the water were extracted for velocity calculations.

The drag and lift forces, coefficients, and wet surface were used to calculate the energy related to the drag and lift forces. The force results showed that the drag force increased when the wave height and frequency were increased, while the lift force increased when the wave height increased, and decreased when the frequency was increased. The same trend was shown in the energy relating to the forces, as they are proportional. The theoretically available energy in the waves was calculated using hydrodynamic principles, and the ratio of energy related to the forces on the sphere to the theoretically available energy was studied. This energy harvesting ratio showed that, unlike the amount of energy from forces, the energy harvesting ratio decreased with increasing wave height, and increased with increasing frequency. This could be due to the wet surface interacting with a smaller area as the wave height increases, leading to a smaller amount of the available energy interacting with the sphere. The increasing frequency is in direct relation to a decrease in the available energy while interacting with the same wet surface. Thus, a larger portion of the available energy is absorbed by the sphere. These results could indicate that spherical wave energy converters are probably not the best-shaped converters for energy harvesting, but could be more resilient to damaging waves.

Contents

Nomenclature

$\bar{\bar{\tau}}$	*Stress tensor*
δ	*Kronecker function*
ϵ	*Turbulent dissipation, Phase shift*
λ	*Wavelength*
μ	*Fluid viscosity*
μ_t	*Turbulent viscosity*
ω	*Specific dissipation, Angular velocity*
ω_e	*Effective angular velocity*
ϕ	*Time-averaged scalar, Velocity potential*
ρ	*Density*
θ	*Angle*
ζ	*Surface elevation*
ζ_a	*Wave amplitude*
A	*Area*
a	*Acceleration*
C_D	*Drag coefficient*
c	*Wave speed*
d	*Water depth*
E_K	*Kinetic energy*
E_P	*Potential energy*
E	*Energy*
F_B	*Buoyancy force*

F_D *Drag force*

F *Force, Fluid volume fraction*

f *Frequency*

g *Gravitational acceleration*

H *Wave height*

h *Wave height, Cap height*

I *Unit tensor*

k_x, k_y, k_z *Wave number for the respective coordinates*

k *Turbulent kinetic energy, Wave number*

P *Wave power*

Q_s *Fluid source*

R, r *Radius*

S *External momentum source*

T *Wave period*

t *Time*

U *Velocity*

u *Velocity*

V *Volume, Velocity, Voltage*

v *Velocity*

x, y, z *Cartesian coordinates*

Equations are cited directly from their references, and therefore, some notations are used for multiple variables.

1 Introduction

The world is undergoing massive changes due to climate change. With an ever-increasing amount of CO2 being released into the atmosphere, the changes are rapidly accelerating. One of the biggest contributors to climate change is the energy sector, emitting more than 36 gigatons of CO2 in 2021 [1]. The world's population is growing, leading to an increased demand for energy. To decrease the amount of CO2 in the atmosphere, while increasing energy production, sustainable new technologies are needed. Today, the three major sources of renewable energy are hydropower, solar energy, and wind energy. Hydropower is the biggest contributor, but the growth rate is the lowest compared to other energy sources. Solar energy, on the other hand, is rapidly expanding as the technology is developing and the energy conversion efficiency is rising. Wind energy is also increasing, with contributions from more installations and better turbines [2].

Wave energy is another source of renewable energy, though it is nowhere as commercialized as the aforementioned. Wave energy could be a massive, mostly untapped resource with an estimated global potential of 2 TW [3]. Nearer to shore, the potential is estimated to be closer to 1.3 TW globally, which is equivalent to a technically exploitable resource of 100-800 TWh/year [4].

Using waves to harness renewable energy has its advantages over other sources of renewable energy. Sea waves offer the highest energy density among renewable energy sources [5]. Also, according to Thorpe, wave power is less environmentally degrading than other forms of energy sources, especially in relation to emissions. Wave energy converters (WECs) produce no solid or fluid emissions, so, during operations, WECs are non-polluting. On the other hand, Thorpe points out that the limited experience with WECs can only give incomplete pictures of the environmental effects, and some effects might be location-specific [6]. A third benefit to harvesting wave energy is that unlike wind and solar power installations, which are only capable of producing 20-30 % of the time, wave energy could produce up to 90 % of the time [7], as solar power is dependent on a clear sky, and wind power is dependent on the wind. Sea waves, on the other hand, are ever present, and therefore, wave power could contribute to more reliability in power supply.

As stated, the field of wave energy is under development. Whereas harvesting energy from ocean waves was previously thought to be unrealistic, several prototypes and some installations are currently available.

While ocean waves carry more potential energy, the rough conditions of the open seas shorten the lifespan of the installations, making commissioning and maintenance difficult and expensive. To make wave energy technology economically attractive, smaller and more resilient converters should be introduced and tested, as was done during the early development of commercial wind energy technology. Seas with lower energy, *i.e.* the Mediterranean Sea, are ideal for this purpose. Advantages to installing converters in the nearshore include protection of ports and coastlines and mitigation of erosion. Disadvantages include negative effects on the aquatic ecosystems from vibrations and low-frequency long-duration noise, but further research is required on this topic. Despite these potential issues, wave energy can increase renewable energy production, create jobs, and advance existing technology [8].

The efficiency of such generators needs to be on a sufficient level if harvesting energy from ocean waves is to be viable. Therefore, this thesis will investigate the percentage of available energy in regular waves that can be absorbed from a spherical object. This will be done using both computational fluid dynamics simulations and with experimental model testing. The parameters to be investigated are:

- Available energy in waves
- Wave loads onto the object
- The corresponding energy to the wave loads
- Percentage of available energy absorbed by the object

This thesis aims to contribute to further research on the optimization of wave energy converters and to be used as input to the ongoing research for more advanced investigations onto the topic, including generator technology, prototype development, and ultimately to contribute towards renewable energy production from a stable source, which could add stability to the future renewable energy mix.

2 Theoretical Background

This section covers the theoretical background of computational fluid dynamics, including turbulence models, the volume of fluid method, and mesh investigation parameters. Further, the relevant hydrodynamic parameters used in this thesis are derived and presented.

2.1 Computational Fluid Dynamics

Computational Fluid Dynamics (CFD) is a fluid dynamics simulation tool used in engineering that allows, among others, for simulating interactions between fluids and objects. It is a powerful tool if used correctly, and allows for predicting parameters like forces, velocity, and pressure, among other things. This can be used for design and optimization, without having to make new experimental models for each refinement. However, as simulations are built on theoretical formulas, like the Navier-Stokes equations, and numerical methods, which have their restrictions, further verification using *e.g.* model testing is required.

This thesis attempts to simulate the interaction between waves and floating objects. It includes multiphase flows with a free surface approach aimed at calculating flow forces. Due to the complexity of this task, the initial simulations are simplified using a 2D domain, to allow for quicker calculations when testing simulation assumptions. These include the solver setup, the solution method, turbulence models, and the interaction between liquid and gas fractions, among others. As the proposed task in this thesis is a complex 3D problem, 2D simulations are not sufficient for force calculations, so 3D model simulations are implemented to account for all physical phenomena.

2.1.1 Navier-Stokes equations

The Navier-Stokes equations are a set of partial differential equations, which are an application of Newton's second law of motion for fluid flows, and the continuity equation for mass and momentum conservation. For incompressible fluids, the mass conservation equation can be written in the general form as shown in Equation 1, and the momentum conservation equation in the general form is shown in Equation 2 [9].

$$\frac{\partial \tilde{\rho}}{\partial t} + \bigtriangledown \cdot \left(\tilde{\rho}\vec{\tilde{v}}\right) = Q_s \tag{1}$$

$$\frac{\partial}{\partial t}\left(\tilde{\rho}\vec{\tilde{v}}\right) + \bigtriangledown \cdot \left(\tilde{\rho}\vec{\tilde{v}}\vec{\tilde{v}}\right) = -\bigtriangledown \tilde{p} + \bigtriangledown \left(\bar{\bar{\tau}}\right) + \tilde{\rho}\vec{g} + \vec{S} \tag{2}$$

The term $\bar{\bar{\tau}}$ is a stress tensor, expressed in Equation 3 [9].

$$\bar{\bar{\tau}} = \mu\left[\left(\bigtriangledown \vec{\tilde{v}} + \bigtriangledown \vec{\tilde{v}}^T\right) - \frac{2}{3}\bigtriangledown \vec{\tilde{v}} I\right] \tag{3}$$

Here, μ is fluid viscosity, I is the unit tensor, $\vec{g}$ is gravity, Q_s is the fluid source, $\vec{S}$ is an external momentum source and $\vec{v}$ is the instantaneous velocity.

The governing equations can not be directly used to simulate the fluid flow. Therefore, one of the widely used approaches in CFD is replacing the instantaneous variables with time-averaged values and fluctuations over those values. This way, any flow scalar can be presented by Equation 4 [10].

$$\tilde{\phi} = \phi + \phi' \tag{4}$$

Here, ϕ is a time-averaged value and ϕ' is the fluctuation over this value. Replacing the instantaneous values with the time-averaged ones, the Navier-Stokes equations are transformed into the Reynolds-Averaged Navier-Stokes (RANS) equations. Equation 5 shows the mass conservation equation and Equation 6 shows the momentum conservation [10].

$$\frac{\partial \rho}{\partial t} + \frac{\partial}{\partial x_j}\left(\rho u_i\right) = 0 \tag{5}$$

$$\frac{\partial}{\partial t}\left(\rho u_i\right) + \frac{\partial}{\partial x_i}\left(\rho u_i u_j\right) = \frac{\partial p}{\partial x_i} + \frac{\partial}{\partial x_j}\left[\mu\left(\frac{\partial u_i}{\partial x_j} + \frac{\partial u_j}{\partial x_i} - \frac{2}{3}\delta_{ij}\frac{\partial u_l}{\partial x_l}\right)\right] + \frac{\partial}{\partial x_j}\left(-\rho\overline{u_i' u_j'}\right). \tag{6}$$

The term $-\rho\overline{u_i' u_j'}$, called the Reynolds stress, must be modeled to close the RANS equations. One of the most common approaches is the Boussinesq approach, which defines the Reynolds stress to the gradient of the mean fluid velocity gradient. This approach is shown in Equation 7 [10].

$$-\rho\overline{u_i' u_j'} = \mu_t\left(\frac{\partial u_i}{\partial x_j} + \frac{\partial u_j}{\partial x_i}\right) - \frac{2}{3}\left(\rho k + \mu_t\frac{\partial u_k}{\partial x_k}\right)\delta_{ij} \tag{7}$$

Here, δ_{ij} is the Kronecker function expressed in Equation 8 [10].

$$\delta_{ij} = \begin{cases} 1 & i = j \\ 0 & i \neq j \end{cases} \tag{8}$$

The turbulent viscosity μ_t can be derived from additional transport equations, called turbulence models.

2.1.2 Turbulence models

There are a lot of different models which can be used to model turbulence. This subsection covers some of the most frequently used turbulence models and their strengths and drawbacks.

k-ϵ

The k-ϵ model is one of the most widely known and used two-equation turbulence models. It uses two extra transport equations to represent the turbulent properties of the flow. Here, the k-equation is the turbulent kinetic energy, while ϵ is the turbulent dissipation, which describes the scale of the turbulence [11].

The k-ϵ model has been shown to be useful for free-shear layer flows with small pressure gradients (*i.e* in an open, wide fluid domain). For wall-bounded flows, the model gives a good agreement with experimental results for zero or low mean pressure gradients but is less accurate for large pressure gradients. The model's predictions do not take into account the free-stream values of the turbulence. The model also requires fine grid spacing/meshing near solid walls [11].

Wilcox's k-ω

Wilcox's k-ω turbulence model is a commonly used two-equation model. This means that the model includes two extra transport equations to represent the turbulent properties of the flow. This allows the model to account for historical effects like convection and diffusion of turbulent energy.

The first variable is the amount of turbulent kinetic energy, denoted with a k, and the second variable ω is the specific dissipation, the variable that determines the scale of the turbulence.

The k-ω model of Wilcox has proven to be superior to the k-ϵ model in viscous near-wall sublayers. In free-shear layer and adverse-pressure-gradient boundary layer flows, the result of the k-ω are sensitive to small free-stream values of ω [11].

SST k-ω

The SST K-ω is a turbulence model which is widely used. The Shear Stress Transport (SST) model combines the use of the k-ω model, which excels in boundary layers close to the wall boundary conditions, with the k-ϵ model's properties in free stream flows, where the k-ω model is known for being too sensitive to the inlet free stream turbulence properties. The drawback of the SST k-ω model is that it produces too large turbulence levels in regions with large normal strain. These regions include stagnation regions (*i.e.* if the diameter of a pipe section decreases), and regions with strong acceleration. However, in this thesis, the spherical object will be placed in a wide fluid domain, and hence, should not be affected by the aforementioned problems with the turbulence model [12].

2.1.3 Volume of fluid method

The Volume of fluid method is used for simulating free surface flows. As this thesis presents a two-phase domain, a method applicable to free surface modeling is used. One of these is the Volume of Fluid method.

Marker-and-Cell method

The Marker-And-Cell (MAC) method was the first computational method created that could handle incompressible, viscous fluids that move non-linearly, developed by Harlow and Welch in 1966. In the MAC method, the fluid flow may have a free surface on which waves can form and break or be fully enclosed within walls. When using the MAC method, the motion of the fluid is calculated by the complete Navier-Stokes equations, with all non-linear terms, with pressure and velocity as the dependent variables [13]. The drawbacks of this method in the modern era include discrete changes in grid element properties when a particle moves between grid elements.

Volume of Fluid Method

The Volume of Fluid (VOF) method is a method of discretization, based on the Marker-and-Cell (MAC) method. The VOF method considers the amount of fluid that passes the boundaries between cells during a time step δt. Globally, the total volume fluctuating is therefore expressed by Equation 9.

$$\frac{\delta F}{\delta t} + \vec{v} \cdot \nabla F = 0 \tag{9}$$

Here, F is the fluid volume fraction, v is the velocity, and t is time. To prevent instabilities or inaccuracies, the VOF method uses an approximation of the free surface, rather than using an exact fluid level [14]. The VOF method is widely used for cases with a two-phase fluid flow, as the case in this thesis.

2.1.4 Domain discretization

In CFD, a fluid domain is discretized into a grid of cells with geometrically simple shapes. Within this grid, the behavior of the fluid is simulated. It is imperative that the grid resolution is sufficiently fine such that the local changes in motion and momentum of the fluid particles change gradually throughout the domain while keeping the resolution as coarse as possible to cut down on computational time.

Whereas the resolution is an important factor in the quality of the mesh, other factors have their influence as well. Some of the most important ones are skewness, the aspect ratio, and the orthogonal quality of the mesh [15]. Furthermore, the shape of the elements and the connection between these control volumes are very important. A quadrilateral (in 2D) or a hexahedral (in 3D) mesh gives a better structure, which in turn makes the calculation increments defined by the control volumes even and smoother. Examples of different element types are presented in Figure 1.

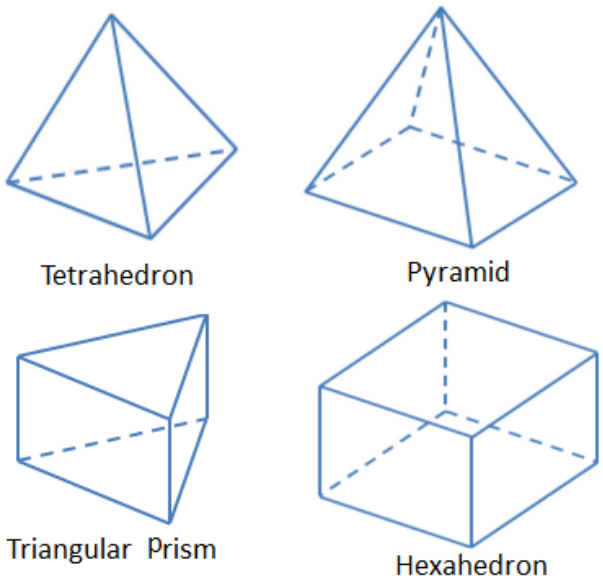

Figure 1: Examples of element types [16]

However, for complex geometries, it can be difficult to create a regular and structured mesh. For example, if one has a circular geometry connected to a quadratic profile, it is hard to keep a hexahedral mesh, especially close to the connection between the two profiles. To combat this, one has two options. Either create a poor and unstructured mesh, consisting of a grid of triangular elements, or create a hybrid mesh. A hybrid mesh is when the regularity of the mesh is kept as structured as possible while allowing some triangular elements with lower structure or some hexahedral elements with higher skewness in transitional areas to connect the geometries in question [15]. A further study into skewness, aspect ratio, orthogonal quality, smoothness, and the y+ value, including limits, are described below:

Skewness

Skewness is a measure used to quantify how much a cell deviates from orthogonality with respect to its faces. It is defined as the difference between the shape of the cell and the shape of an equilateral (*i.e.* all sides are of the same length) cell of an equivalent volume. Highly skewed cells could decrease the accuracy and stability of the solution. In general, the maximum skewness of the mesh should be below 0.95, with an average value below 0.33 [15].

Aspect ratio

The aspect ratio is a measure of the stretching of a cell. It is defined as the ratio of the maximum value to the minimum value of either the distance between the center of the cell and the center of the face or the distance between the cell center and the nodes. The aspect ratio should be kept as low as possible, and not above 35:1 [15].

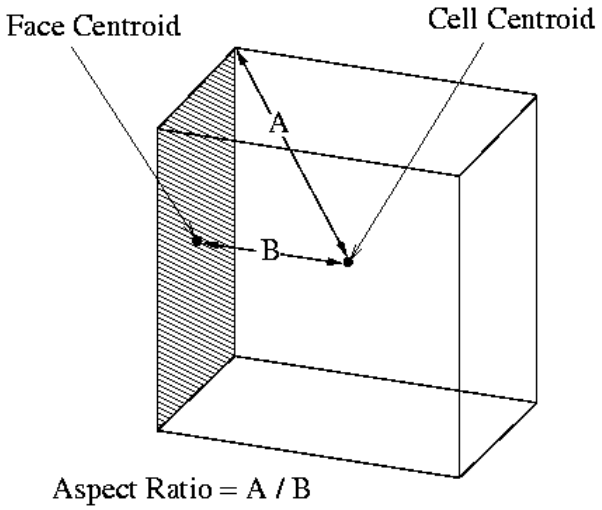

Figure 2: Mesh aspect ratio visualized [15]

Orthogonal quality

The orthogonal quality is computed by creating a vector from the centroid of the cell to each of the faces, from the centroid of the cell to the centroid of the adjacent cells, and the face area vector. The orthogonal quality is a parameter between 0 and 1, where 0 indicates low-quality cells and 1 indicates high-quality cells [15].

Smoothness

For the smoothness of the mesh to be good, the change in the fluid parameters, like the velocity, the direction vector, and the density, should change gradually between the control volumes. If the gradient between adjacent cells is too high, computational errors can occur. To avoid this, the control volumes should not change rapidly [15].

y+

The y+ value is a dimensionless distance from the wall of the first mesh node and determines whether the influences in the wall adjacent cells are laminar or turbulent. This is used to describe whether the mesh is fine or coarse. y+ values are divided into 3 subcategories; viscous sublayer with y+ < 5, where the velocity profile is assumed to be laminar and dominate the wall shear, $5 \leq$ y+ < 30, where the velocity profile is assumed to dominate both viscous and turbulent shear, and $30 \leq$ y+ < 300, where turbulent shear dominates. For wall functions, a y+ value of ≈ 30 is desirable, whereas a y+ value of ≈ 1 is the best for near wall modeling [17].

2.1.5 Implicit and explicit methods

The implicit and explicit methods are numerical analysis methods used to solve the Navier-Stokes equations. The explicit method calculates the system status at a future time step, while the implicit method takes the current time step as well as the future time step. As the explicit method does not take into account the current time step, the solution is less stable. This means that unless the time steps are significantly small, explicit solutions are at risk of diverging. These differences are explained mathematically in Equation 10 for the explicit method and Equation 11 for the implicit method.

$$y_{n+1} = y_n + hF(y_n, t_n) \tag{10}$$

$$y_{n+1} = y_n + hF(y_{n+1}, t_{n+1}) \tag{11}$$

These equations show that the implicit method has the *n+1* terms of the right side of the equation, as well as the y_n. This creates a smoother transition between time steps, which is more stable and opens up for larger time step sizes. On the other hand, this is a more complex solution method, which requires more computational power [18].

2.1.6 Transient and steady-state problems

CFD simulations can be conducted for steady-state or transient conditions. A steady-state flow is a flow where the flow conditions do not change with time. A transient flow, on the other hand, allows for flow conditions that vary with time. The problem proposed in this thesis is a multiphase flow simulation of waves interacting with a submerged object. Therefore it is considered a transient problem.

2.1.7 Pressure-velocity coupling algorithms

The simulation software offers five algorithms to solve the coupling between velocity and pressure. The three used during the model preparation are listed in this subsection.

Semi-Implicit Method for Pressure-Linked Equations (SIMPLE)

The SIMPLE method is the default solver scheme in Fluent. This algorithm is considered robust, fast and rarely creates divergence in the fluid domain [15].

Pressure-Implicit with Splitting of Operators (PISO)

The Pressure-Implicit with Splitting of Operators method, commonly known as the PISO method is a solver method that is useful for unsteady flow problems or for domains with higher than average skewness. The PISO algorithm is based on a higher degree of approximation of the relation between pressure and velocity. The PISO algorithm applies corrections between neighboring cells to offer a smoother and more accurate solution. At the same time, this connection between cells makes the algorithm vulnerable to large changes in the domain, and hence, it is dependent on smaller changes between time steps, *i.e.* on small time step sizes to avoid divergence [15].

Coupled

The coupled algorithm gives a robust and efficient solution for steady-state problems. For transient cases, the robustness of the coupled method gives faster convergence and does not easily diverge if the mesh is poor or the time steps are larger [15].

2.2 Hydrodynamics

2.2.1 Water level calculation

To calculate certain wave parameters, hydrodynamic properties must be taken into the equation. To determine whether the water depth is defined as shallow, intermediate, or deep is defined in Equations 12-14.

$$d/\lambda \leq 0,05 \Rightarrow shallow \tag{12}$$

$$0,05 < d/\lambda < 0,5 \Rightarrow intermediate \tag{13}$$

$$d/\lambda \geq 0,5 \Rightarrow deep \tag{14}$$

Here, d is the water depth and λ is the wavelength.

2.2.2 Calculating the wavelength

Calculating the wavelength depends on whether the waves are in shallow, intermediate, or deep water. For deep water, the wavelength can be calculated using Equation 15.

$$\lambda_d = \frac{gT^2}{2\pi} \tag{15}$$

Here, λ_d is the deep water wavelength, g is the acceleration due to gravity and T is the wave period. For intermediate water depth, the approach is different. First, one calculates the deep water wavelength. Then, based on this result, one iterates using Equation 16 until the wavelength stabilizes [19].

$$\lambda = \frac{gT^2}{2\pi} tanh\Big(\frac{2\pi d}{\lambda}\Big) \tag{16}$$

Here, λ is the wavelength, g is the acceleration due to gravity, T is the wave period, and d is the water depth. For shallow water, the wavelength can be calculated using Equation 17 [19].

$$\lambda_s = \sqrt{gd}\, T \tag{17}$$

Here, g is the acceleration due to gravity, d is the water depth and T is the wave period [19].

2.2.3 Calculating the wave speed

The equations used for calculating the wave speed depend on whether the waves occur in deep, intermediate, or shallow waters. For deep water, the wave speed can be calculated using Equation 18 [19].

$$c_d = 1,56T \tag{18}$$

Here only the wave period T is needed. For intermediate depths, the wave speed is calculated using Equation 19 [19].

$$c = \frac{gT}{2\pi} tanh\Big(\frac{2\pi d}{\lambda}\Big) \tag{19}$$

Here, g is the acceleration due to gravity, T is the wave period, d is the water depth and λ is the wavelength. For shallow waters, the wave speed only depends on the acceleration due to gravity and the water depth, as shown in Equation 20 [19].

$$c_s = \sqrt{gd} \tag{20}$$

If the wavelength is known, then the speed can be calculated using the relation given in Equation 21.

$$v = f\lambda \tag{21}$$

2.2.4 Archimedes' principle

Archimedes' principle is used to determine the buoyancy of an object. This is important to calculate such that the model can be sufficiently ballasted to ensure equilibrium in the desired position. The buoyancy force is calculated using Equation 22.

$$F_b = \rho g V \tag{22}$$

Here, F_B is the buoyancy force, ρ is the density of the fluid, and V is the submerged volume of the object.

2.2.5 Available energy in waves

Beneath waves in deep waters, the water particles rotate in circular paths with an angular velocity ω and a radius of $\zeta_a e^{kx}$, where ζ_a is the wave amplitude [m], k is the wave number [m^{-1}], and x is the position [m]. The kinetic energy of a mass particle is described in equation 23, assuming one length unit in the y-direction [19].

$$dE_K = \frac{1}{2}\rho dx dz V^2 \tag{23}$$

$$= \frac{1}{2}\rho dx dz \Big[\Big(\frac{\delta\phi}{dx}\Big)^2 + \Big(\frac{\delta\phi}{dz}\Big)^2\Big]$$

$$= \frac{1}{2}\rho\omega^2\zeta_A^2 e^{2kz} dx dz$$

Here, ρ is the density of the fluid, and V is the velocity. The total kinetic energy over a wavelength in deep water is therefore described by Equation 24 [19].

$$E_K = \int_{-\infty}^{0} dz \int_0^{\lambda} \frac{1}{2}\rho\omega^2\zeta_A^2 e^{2kz} dx \tag{24}$$

$$= \frac{1}{2}\rho\omega^2\lambda\zeta_A^2\frac{1}{2k}$$

Since $\omega^2 = \mathrm{k} \cdot \mathrm{g}$ for deep waters, Equation 24 can be rewritten into Equation 25 [19].

$$E_K = \frac{1}{4}\rho g\zeta_A^2\lambda \tag{25}$$

This relation is also valid for intermediate water depths [19].

The mass particle also has potential energy, as it is lifted from its initial still-water position. At the surface, the fluid element dx has the potential energy described by Equation 26 [19].

$$dE_P = \rho g(dx\zeta)\frac{1}{2}\zeta \tag{26}$$

Over a wavelength, the potential energy is expressed with Equation 27, based on Equation 26 [19].

$$E_P = \int_0^{\lambda} \frac{1}{2}\rho g \zeta^2 dx \tag{27}$$

$$= \frac{1}{4}\rho g \zeta_A^2 \lambda$$

This is valid for deep and intermediate water depths. The total energy per unit width and for any water depth is therefore described by Equation 28 [19].

$$E = E_K + E_P = \frac{1}{2}\rho g \zeta_A^2 \lambda \tag{28}$$

2.2.6 Calculating harvestable energy from numerical data

The harvested wave power can be calculated using Equation 29.

$$P = F \cdot U \tag{29}$$

Here, F is the force, and U is the velocity. By integrating this term over the wave period, the energy over one wavelength can be calculated with Equation 30.

$$E = \int_0^T P \, dt = \int_0^T F \cdot U \, dt \tag{30}$$

To calculate the velocity of the waves from the numerical data, some data processing is needed. These are shown in Figure 3.

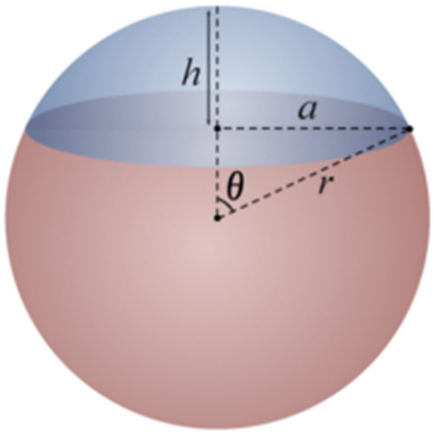

Figure 3: Sphere with relations for velocity calculations

The total area of a sphere is defined by Equation 31, and the cap area, as shown in Figure 3, *i.e.* the unsubmerged area is given by Equation 32.

$$A_{Total} = 4\pi r^2 \tag{31}$$

$$A_{Cap} = 2\pi r h \tag{32}$$

The cap height (h), can be calculated by Equation 33.

$$h = \frac{A_{Total}}{A_{Cap}} \cdot 2r \tag{33}$$

In order to calculate the projected area for the drag force direction, A_{green}, (shown in green in Figure 4) the following equations can be used.

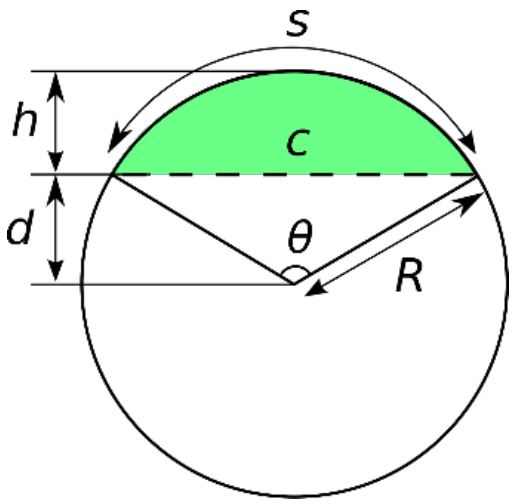

Figure 4: Circular area with relations

The length c is defined in Equation 34, θ is defined by Equation 35, and the area of the green section is given by Equation 36.

$$c = 2\sqrt{R^2 - (R-h)^2} \tag{34}$$

$$\theta = 2\arcsin\left(\frac{c}{2R}\right) \tag{35}$$

$$A_{Green} = \frac{R^2}{2}(\theta - sin(\theta)) \tag{36}$$

From these relations, the projected areas with respect to the drag and lift directions are given in Equation 37 and Equation 38 respectively.

$$A_{Drag} = \frac{r^2}{2}(\theta - sin(\theta)) \tag{37}$$

$$A_{Lift} = \frac{\pi c^2}{4} \tag{38}$$

Using Equation 39 [19], the effective velocity (U) can be calculated by Equation 40.

$$F = \frac{1}{2}\rho C_D A U^2 \tag{39}$$

$$U = \sqrt{\frac{2F}{\rho C_D A}} \tag{40}$$

Here, C_D is the drag coefficient, A is the projected area normal to the velocity direction and ρ is the water density.

2.2.7 Defining waves in ANSYS Fluent

When defining a wave in ANSYS, it calculates the input using the governing equation shown in Equation 41 [15].

$$\zeta = \zeta_A cos(k_x x + k_y y - \omega_e t + \epsilon) \tag{41}$$

Here, ζ_A is the wave amplitude, ϵ is the phase difference, k_x and k_y are the wave numbers in their respective directions. The wave number is defined in Equation 42 and ω_e is the effective wave frequency, defined in Equation 43 [15].

$$k = \frac{2\pi}{\lambda} \tag{42}$$

$$\omega_e = \omega + kU \tag{43}$$

Here, λ is the wavelength and U is the uniform incident wave velocity. The effective frequency is a Doppler shifted wave frequency, where the observer is traveling with the base flow U, unlike the absolute frequency, where the observer is static in the coordinate system [20]. Here, the absolute frequency ω is defined in Equation 44.

$$\omega = \sqrt{gk \cdot tanh(kh)} \tag{44}$$

Following, the velocity components can be derived for shallow/intermediate waves, using Equation 45 [15].

$$\begin{pmatrix} u \\ v \end{pmatrix} = \frac{gk\zeta_a}{\omega} \frac{cosh[k(z+h)]}{cosh(kh)} \begin{pmatrix} cos\theta \\ sin\theta \end{pmatrix} cos(k_x x + k_y y - \omega_e t + \epsilon) \tag{45}$$

Here, g is gravitational acceleration, k is the wave number, ζ_a is the wave amplitude, ω is the angular frequency, t is time, ϵ is phase shift and x, y, and z are cartesian coordinates. As the inlet is defined in the x-direction, only the definition of u will be used. Also, the inlet uses the maximum value of u, and therefore, the cosine link and the hyperbolic cosine fraction are assumed to be equal to 1. At the inlet boundary condition, ANSYS requires a velocity input, wave height, and wavelength. To create the proper wave, the effective wave frequency will have to match the desired frequency output.

3 Numerical Simulations

To prepare the model, a 2D adaption is used to keep simulation time low while testing the input parameters. While a 2D model will make test simulations go significantly faster, it is not a good adaption for numerical calculations for this case, as a sphere in a two-dimensional space is a cylinder. Nevertheless, to check that the input parameters create the desired output wave, and to test the performance of the implicit versus explicit method and the performance of the pressure-velocity coupling algorithms, this adaption is adequate. To get reliable and accurate data, the results from the 2D simulations are used to create a suitable 3D adaptation.

This section will cover the process of creating a domain, discretizing the domain into a fine grid of cells, analyzing the resulting mesh, and setting up the boundary conditions, solution models, and initialization and solver settings.

The following assumptions are valid for all simulations:

- Fluid properties are constant
- Incompressible flow
- Homogeneous phases
- No heat transfer
- No mass transfer
- No surface tension between phases

3.1 Preparing CFD Model

3.1.1 Fluid domain

The fluid domain is defined as a rectangular domain with the dimensions shown in Table 1.

Table 1: Domain parameters for the 2D fluid domain

Parameter	**Value**
Length in x-direction [m]	15
Height in z-direction [m]	4.5
Sphere diameter [mm]	200
Still water level [m]	2.5

These dimensions are coherent with the wave tank at the experimental testing facility, although the domain length is reduced. This is done to reduce the computational power and time needed while leaving enough room for the waves to build up before reaching the object, and enough room after the object for the waves to not be reflected back at the end of the domain. The sphere is placed at $x = 10$ m and is defined by removing a cylindrical hole from the fluid domain. The edge of the cutout is defined as a no-slip wall. The fluid domain is presented in Figure 5.

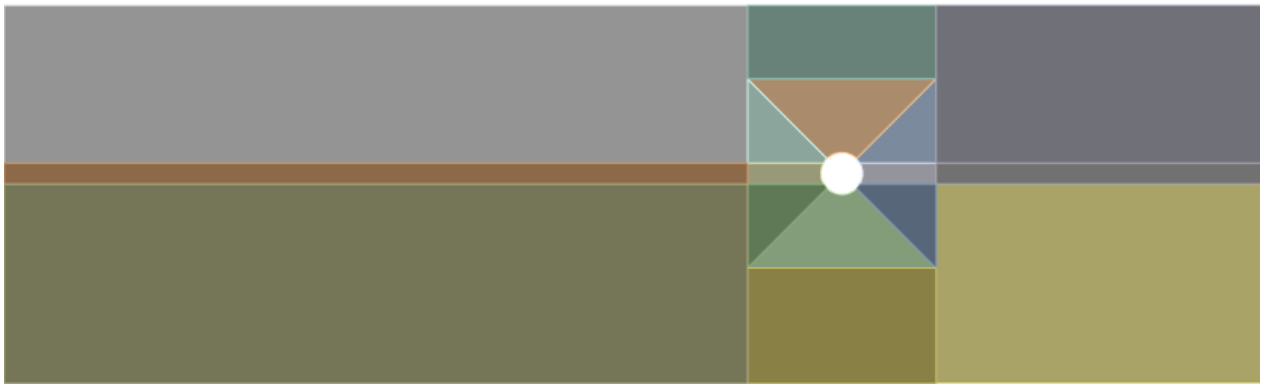

Figure 5: 2D Fluid domain

As this figure shows, the fluid domain is sliced into different sectors. These will be used to refine the mesh in the areas requiring higher accuracy.

3.1.2 2D mesh

To create a good mesh, the mesh type is set to quadrilateral, and the domain is discretized into elements of size 200 mm each. This gives the mesh details given in Table 2.

Table 2: Mesh details for the 2D mesh

Parameter	**Value**
Element size [mm]	200
Number of nodes	10557
Number of elements	10279

Edge sizing is used in the sliced sectors of the fluid domain to refine the mesh in the wave channel and close to the object. Figure 6 shows the sectors which are given this treatment.

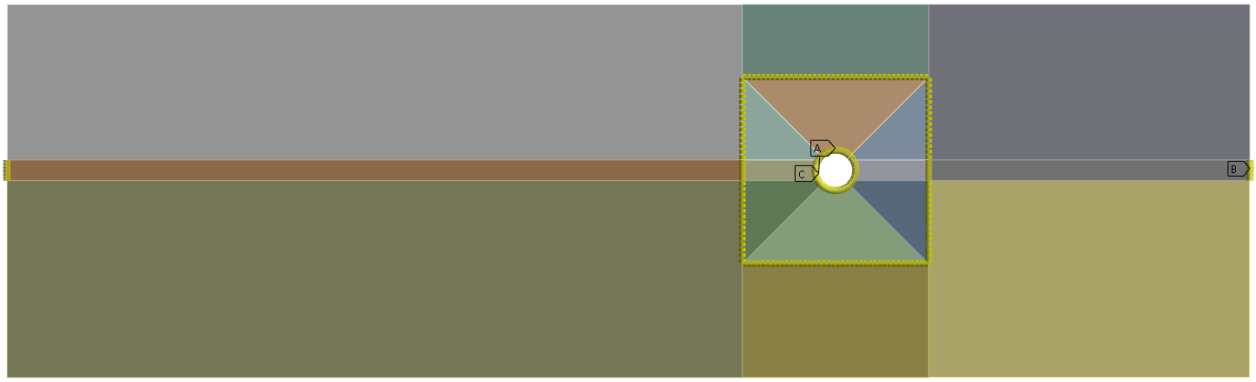

Figure 6: Edge sizing used for meshing

Here, edge sizing A divides the top and bottom of the sphere, as well as the horizontal slices above and below the sphere into 40 divisions. Edge sizing B divides the horizontal channel through the sphere, as well as the side walls of the sphere, into 30 divisions. Edge sizing C divides the vertical slices around the sphere, except the channel controlled by edge sizing B. Edge slicing C also controls the point where the diagonal lines meet the sphere. Edge slicing C divides these features into 15 divisions. Figure 7 shows the full fluid domain after meshing.

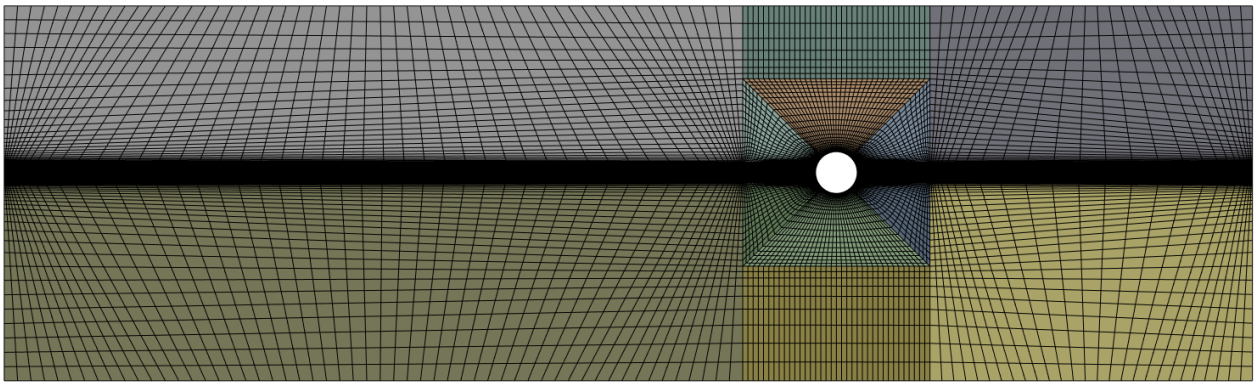

Figure 7: Mesh after the edge sizing

The mesh quality is determined by looking at the aspect ratio, skewness, and orthogonal quality. These parameters are explained thoroughly in the theory section and are given in ANSYS meshing. The minimum, maximum, average, and standard deviation of these parameters are given in Table 3.

Table 3: Mesh quality parameters for the 2D mesh

	Aspect ratio	**Skewness**	**Orthogonal quality**
Min	1.0	$1.3 \cdot 10^{-}3$	0.72
Max	59.4	0.5	1.00
Average	15.3	0.1	0.97
Standard deviation	23.3	0.1	0.10

As stated in the theory section, the aspect ratio should be below 35. Here, the average is below said value, but the maximum is above. Figure 8 shows where the cells with the maximum aspect ratio are located.

Figure 8: High aspect ratio cells for the 2D mesh

As the figure shows, the cells with an exceeding aspect ratio are located in the wave channel, which is not ideal, but the aspect ratio drops below the maximum recommended value around the point of contact. Therefore, for a test model, it is accepted.

The average skewness of the cells is recommended to be below 0.33, with a recommended maximum below 0.95. Table 3 shows that the average skewness is well below the recommended 0.33, and the maximum is not close to the recommended maximum of 0.95.

As Table 3 shows, the average orthogonal quality is high, around 97 %, with a minimum of 0.72. It is expected that some cells have a lower orthogonal quality due to the mesh definitions. As Figure 7 shows, there are diagonal cells before and after the sphere's location, which will naturally be of a lower orthogonal quality, but as they are located away from the waves and point of contact with the object, it is not considered a problem.

3.1.3 2D Solver setup

The domain consists of a primary phase of air and a secondary phase of water, with a density set to 1.225 kg/m^3 and 998.2 kg/m^3 respectively. At the inlet, the open channel wave boundary condition is activated, and the wave pattern is created using the shallow/intermediate wave setting, solved using third-order Stokes wave theory, which is applicable to the wave parameters. In the multiphase options, the wave height and wavelength are input. The wave height is defined for each test, and the related wavelength is calculated using the iterative dispersion relation. This process is described in section 2.2.7.

The outlet boundary condition momentum is kept at the default settings (backflow turbulent intensity [%] = 5 and backflow turbulent viscosity ratio = 10). In the multiphase tab, the open channel option is activated, the free surface level is set to 2.5 m, *i.e.* the still-water level, and the bottom level is set to 0 m. The density interpolation method is kept as "from neighboring cell".

The solution is initialized using standard initialization, with the open channel initialization computed from the inlet, with a flat open channel initialization method.

For testing and preparation, the simulation is run for a varying amount of time steps, with a time step size of 0.01 to 0.05 s with a maximum of 10-20 iterations per time step, depending on the test. The parameters tested in the preparation stage are the effect of calculating using implicit versus explicit methods, different solver settings, and different waves.

3.2 Creating a 3D Model

3.2.1 3D fluid domain

As a result of the model preparation tests, five different fluid domains are created to optimize the calculations. These are created to place the sphere at the position $x = \lambda/2$, to ensure enough room for a damping zone of 2λ after the sphere to avoid reflecting waves and to have a margin between the sphere and the damping zone. To account for these parameters, the fluid domains are given a length of 3λ. As there are 14 waves in total, with five different frequencies and six different wave heights, a fluid domain is created for each of the frequencies. The dispersion relation shown in Equation 16 is used to calculate the wavelength when d/λ is between 0.05 and 0.05, while 15 is used to calculate the wavelength when d/λ is over 0.5. These equations depend on the frequency or period, and not on the wave height. The wavelengths, the ratio of water depth to wavelength, and corresponding fluid domain lengths are presented in Table 4.

Table 4: Wavelengths and fluid domain lengths from their respective frequencies

Frequency [Hz]	**Wavelength [m]**	**d/λ**	**Fluid domain length [m]**
0.3	14.0	0.18	42
0.4	9.2	0.27	27.6
0.5	6.2	0.40	18.6
0.6	4.3	0.58	12.9
0.7	3.2	0.78	9.6

Each fluid domain is sliced around the sphere and the channel for incoming waves to create zones where the mesh can be refined. The domains are also sliced in half along the x-z plane, and the sliced surface is given the symmetry attribute. The y and z dimensions are equal for all of the domains and are defined so that the computational power required is low while keeping them big enough to avoid wall effects interfering with the sphere. The still water level and the sphere diameter, which are the same that will be used for experimental tests, are the same for each domain. These dimensions are shown in Table 5.

Table 5: Fluid domain parameters for the first 3D fluid domain

Parameter	**Value**
Length in x-direction [m]	10
Width in y-direction [m]	3
Height in z-direction [m]	4.5
Sphere diameter [mm]	200
Still water level [m]	2.5
Sphere position from inlet for f = 0.3 Hz [m]	7
Sphere position from inlet for f = 0.4 Hz [m]	4.6
Sphere position from inlet for f = 0.5 Hz [m]	3.1

For a spherical object, the biggest difference between the 2D and 3D simulations is related to the shape. As discussed in the previous section, it is impossible to model a sphere in a 2D domain, as the resulting object is a cylinder, if extrapolated to 3 dimensions. Also, in a 2D fluid domain, all the incoming water is forced to go over the object. When the fluid domain is given the third dimension, the water can both go over the sphere and be deflected to the sides.

3.2.2 3D mesh

When meshing the domain, the element size is set to 150 mm. The same edge sizing and slicing applied to the 2D domain, are used for the 3D domain to refine the mesh in the wave channel and closer to the point of impact. The mesh details are presented in Table 6.

Table 6: Mesh details for the 3D model

Mesh parameter	**f = 0.3 fluid domain**	**f = 0.4 fluid domain**	**f = 0.5 fluid domain**
Element size [mm]	150	150	150
Number of nodes	980352	656390	502178
Number of elements	940965	628881	480128

The resulting mesh graphics from these details are presented in Figure 9, with a closer zoom around the sphere shown in Figure 10. As the same slicing, element sizes and refinements are used, only the mesh from the f = 0.3 Hz model is shown in these figures.

Figure 9: 3D mesh for the full domain

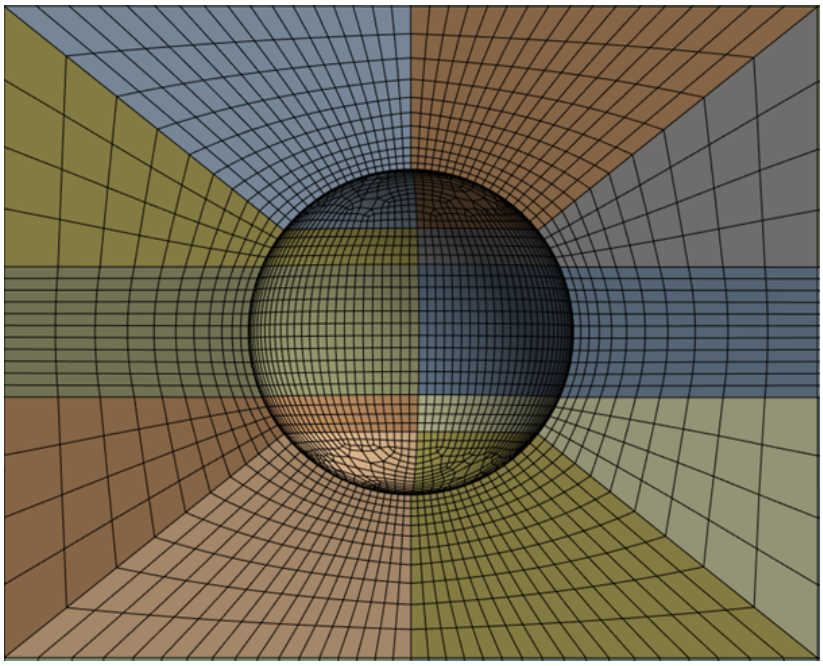

Figure 10: 3D mesh zoomed around the sphere

To analyze the quality of this mesh, the aspect ratio, skewness, and orthogonal quality of the mesh are checked for each fluid domain. These parameters are described in the theory section.

Mesh parameters for the f = 0.3 Hz fluid domain mesh

The minimum, maximum, average, and standard deviation of the aspect ratio, skewness, and orthogonal quality are shown in Table 7.

Table 7: Mesh quality parameters for the f = 0.3 Hz fluid domain

	Aspect ratio	**Skewness**	**Orthogonal quality**
Minimum	1.00	$1.32 \cdot 10^{-10}$	0.15
Maximum	35.93	0.89	1.00
Average	8.76	0.19	0.91
Standard deviation	5.92	0.24	0.17

As Table 7 shows, the average aspect ratio is well below the recommended maximum of 35, but the maximum is slightly above. The cells with the maximum aspect ratio are shown in Figure 11.

Figure 11: Cells with high aspect ratio for the mesh

As the figure shows, these cells are not located in the wave channel, and they are not close to the sphere. As the overshoot in aspect ratio was slight, and not in these more sensitive areas, it is not considered a problem.

Table 7 shows that the average skewness is below the recommended maximum of 0.33, and the maximum skewness stays within the recommended maximum of 0.95.

For orthogonal quality, Table 7 shows the average orthogonal quality is 91 % which is good. The minimum value of 0.15 is expected as the cells go diagonally away from the sphere and wave channel, and these cells have the smallest orthogonal quality. As these cells are not interfering with the sensitive areas of the domain, they are unproblematic.

Mesh parameters for the f = 0.4 Hz fluid domain mesh

The minimum, maximum, average, and standard deviation for the aspect ratio, skewness, and orthogonal quality are shown in Table 8.

Table 8: Mesh quality parameters for the f = 0.4 Hz fluid domain

	Aspect ratio	**Skewness**	**Orthogonal quality**
Minimum	1.00	$1.32 \cdot 10^{-10}$	0.15
Maximum	58.91	0.90	1.00
Average	7.98	0.20	0.92
Standard deviation	5.13	0.19	0.17

As the data shows, the average aspect ratio is well below the recommended maximum of 35, but the maximum exceeds this threshold. The cells with the maximum aspect ratio are shown in Figure 12.

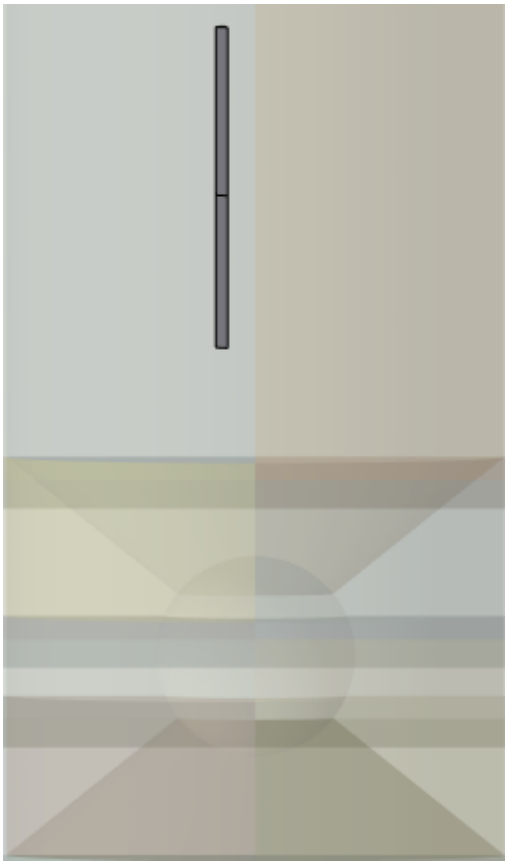

Figure 12: Cells with high aspect ratio for the mesh

As the figure shows, these cells are not located in the wave channel, and they are not close to the sphere. As the cells overshooting the maximum recommended aspect ratio are few, and not in these more sensitive areas, they are not considered problematic.

Table 8 shows that the average skewness is below the recommended maximum of 0.33, and the maximum skewness stays within the recommended maximum of 0.95.

As for the orthogonal quality, Table 8 shows that the average orthogonal quality is 92 % which is satisfactory. A minimum of 0.15 is expected as the cells go diagonally away from the sphere and wave channel, and these cells are located in the same place as for the f = 0.3 Hz mesh. As these cells are not interfering with the wave channel or the sphere, it is not concerning.

Mesh parameters for the f = 0.5 Hz fluid domain mesh

Table 9 shows the aspect ratio for the mesh.

Table 9: Mesh quality parameters for the f = 0.5 Hz fluid domain

	Aspect ratio	**Skewness**	**Orthogonal quality**
Minimum	1.00	$1.32 \cdot 10^{-10}$	0.17
Maximum	43.48	0.93	1.00
Average	7.88	0.17	0.92
Standard deviation	5.03	0.19	0.16

As the table shows, the average aspect ratio is well below the recommended maximum of 35, but the maximum exceeds this value. The cells with the maximum aspect ratio are shown in Figure 13.

Figure 13: Cells with high aspect ratio for the mesh

This figure shows that these cells are not located in the wave channel, and they are not close to the sphere. As the cells overshooting the maximum recommended aspect ratio are few, and not in these more sensitive areas, it is not considered problematic.

Table 13 shows that the average skewness is below the recommended maximum of 0.33, and the maximum skewness is well within the recommended maximum of 0.95.

Table 13 shows that the average orthogonal quality is 92 %, which is good. A minimum of 0.15 is expected as the cells go diagonally away from the sphere and wave channel, and unlike for the other fluid domains, these cells appear after the sphere, and not near the wave channel. Therefore, it is not considered a problem.

3.2.3 3D solver settings

For the Fluent setup, the implicit Volume of Fluid method is utilized as tests using the explicit method frequently diverged, causing "floating point exception" errors, *i.e.* errors due to illegal operations in the governing equations, like attempting to divide by 0.

Further, as mentioned in the fluid domain section, a damping zone called a numerical beach is added to the end of the domain to dampen the waves and as such, avoid backflow from the end of the domain. As Fluent recommends, this damping zone is 2λ long and starts from the end of the domain.

The materials in the fluid domain are defined as air with a density of 1.225 kg/m^3 as the primary phase and liquid water with a density of 998.2 kg/m^3.

For the boundary condition, in the momentum tab of the inlet, the velocity for all cardinal directions is set to zero, as this thesis does not focus on the effect of current. In the multiphase tab, the wavelengths and wave heights are entered, as well as the free surface level, more commonly known as the still water level. The rest of the parameters in these boundaries are left at the default values. The sides and bottom of the fluid domain are given the no-slip wall property, meaning that the fluids are not allowed to move freely along these boundaries. This is especially important for the bottom of the domain, as this is to serve as the seabed for the intermediate waves. The top is set as a free slip wall and not an opening, meaning that it is considered a wall, but the fluids are allowed to move freely along the boundary, with no friction. This is due to early tests showing an inexplicable pressure column going from the free surface level to the top of the domain.

Five report files are defined for further analysis. These are the drag force data along the wave direction, lift force data in the z-direction, their respective drag and lift coefficients, and the water volume fraction at the sphere, *i.e.* the wet surface. The force reports will be used to analyze force results, while the coefficients and wet surface will be used for wave velocity analyses and subsequently for energy calculations.

The solver is set to use the PISO method described in the theory section, as early tests showed that the PISO and coupled algorithms both gave reliable force calculations. However, the PISO method gave quicker simulations. The SIMPLE method was not as reliable, and for certain wave cases, the solution diverged.

The solution is initialized from the inlet using the flat initialization method. This means that the first state before running the waves will be still water. One could initialize using the wavy initialization method to get wave data without having to wait for the waves to reach the sphere. However, to avoid any possibility of generating initial disconnected waves, the extra computational time was allocated to the flat initialization method.

The solution is set to run for a maximum of 8000 time steps of 0.01 s each, and a maximum of 20 iterations per time step. Early tests showed that the solution converged between 10 and 20 iterations, sometimes quicker, so a maximum of 20 iterations is deemed sufficient. The solution is saved every 30 time steps for f = 0.3 Hz, every 25 time steps for f = 0.4 Hz, and every 20 time steps for f = 0.5 Hz to ensure that the solution is sampled at least 10 times per wave.

4 Experimental Method

This section covers the experimental method used in this thesis. The test facility at HVL, MarinLab, the test setup, the equipment used, and the calibration of the measurement equipment are presented in their respective subchapters.

4.1 The MarinLab Test Facility

MarinLab is the hydrodynamic test facility located at HVL campus Bergen, built in 2016. The facility features a 2.2 m x 3 m cross-section tank with a length of 50 m. A model of MarinLab is shown in Figure 14.

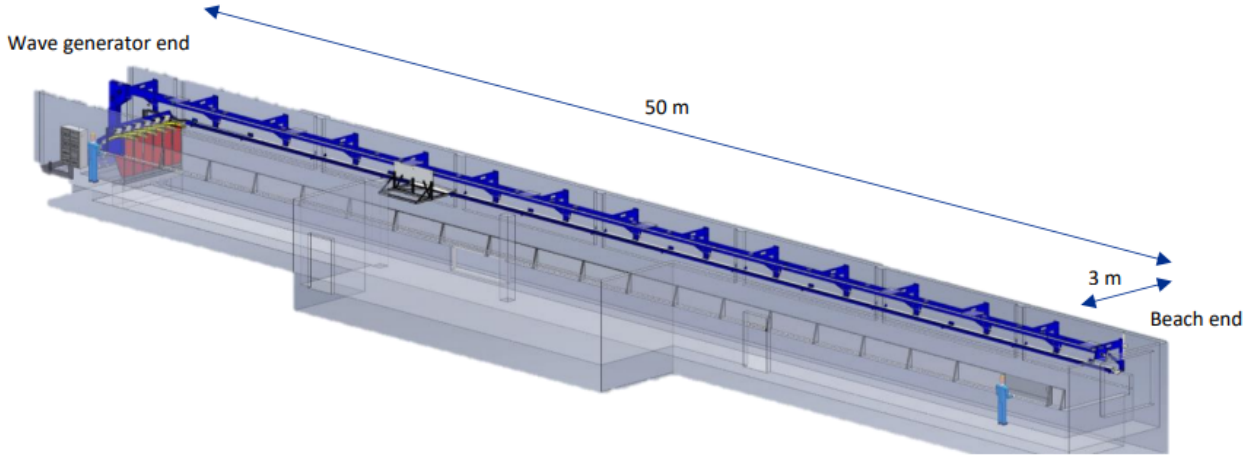

Figure 14: Overview of MarinLab [21]

The tank has a towing carriage from Edinburgh Designs, which has a maximum speed u_{max} = 5 m/s, and a maximum acceleration a_{max} = 1.2 m/s^2. The wave generator consists of 6 hinged wave paddles, which can generate waves with a maximum height of 0.5 m at wave periods close to 2 s. The paddles are force-feedback controlled which allows damping of unwanted wall reflections. The paddles can generate regular waves and irregular waves using JONSWAP, Bretschneider, and Pierson-Moskowitz spectra [21].

On the opposite side of the wave paddles, a passive beach is installed. This beach is made of a metal plate with holes, placed at an angle of 8° to the still water line. This allows for a representative study of wave breaking due to depth change, and it absorbs the incoming waves to counteract reflections. In this thesis, the latter is important to prevent interference from reflecting waves.

The possible waves generated by the paddles must be below the wave-breaking limit curve, shown in Figure 15.

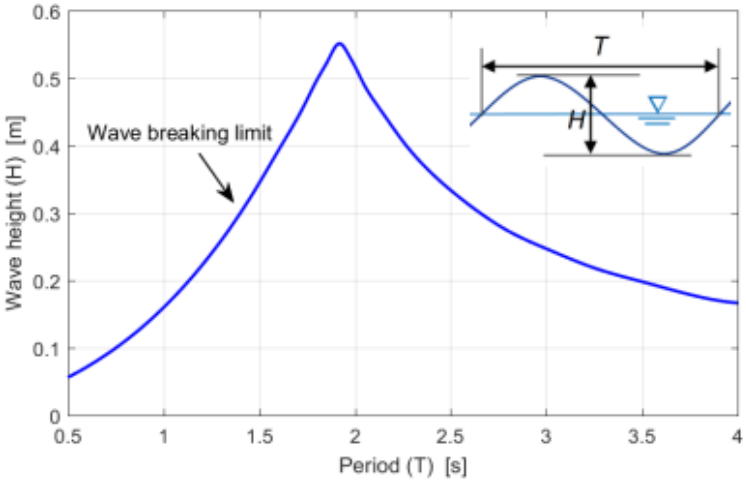

Figure 15: Limit for breaking waves by wave height and period [21]

In addition, MarinLab has the following experimental features:

- Towing Carriage, $u_{max} = 5$ m/s, $a_{max} = 1.2$ m/s^2
- Constant-force towing line
- Qualisys motion capture system
- 8 Resistance-type wave gauges
- Load cells ranging from 5-500 N
- Nortek Acoustic-Doppler Velocimeter
- GoPro underwater cameras for video capture

4.2 Equipment

As stated in section 2.1, it is important to experimentally verify the numerical simulations. The test setup consists of a 40x40 mm AluFlex profile, attached to a spherical buoy. The profile is attached to the buoy using a custom-made aluminum plate. The plate is drawn in the CAD software Creo Parametric and exported to a plasma burner which burns the plate from an aluminum sheet with 5 mm thickness. After the aluminum shape is cut out, the edges are sanded down, and holes for M8 bolts are drilled out. The design for the plate is presented in Figure 16.

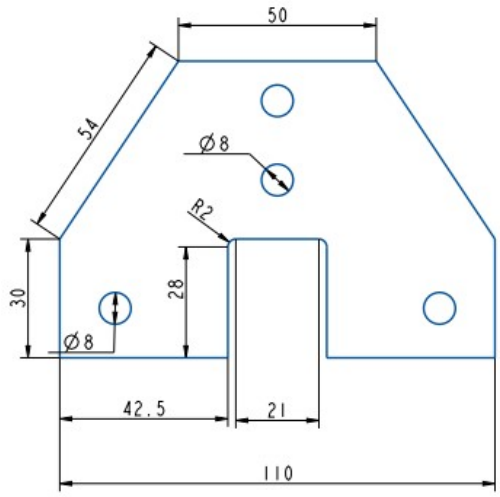

Figure 16: Custom designed plate to attach the buoy to the AluFlex profile. The plate has a thickness of 5 mm

The AluFlex profile is attached to two load cells, which are placed perpendicular to each other, to measure the loads in x- and z-directions. The load cells measure drag and lift force, respectively.

Usually, one would ballast the test model to counteract the buoyancy of the air-filled object. In this case, there are concerns about the structural integrity of the spherical buoy, should an opening be cut out to ballast it. Therefore, a simplification is made. The sphere will be held in the correct position by the AluFlex profile, which is attached to the MarinLab carriage. This means that before the waves apply extra loads to the sphere, and subsequently the load cells, the load cell recording the z-direction loads will record an initial load corresponding to the buoyancy force, minus the weight of the profile itself. This will be accounted for by zeroing the load cell after mounting the experimental setup.

For the experimental setup, a variety of equipment is used. Load cells are used to measure the loads onto the sphere, wave gauges are used to control the wave shape, data acquisition units (DAQ) to sample the data, and various software.

Load cells are measurement devices made for measuring loads. The load cells used in this thesis are S-beam load cells and a button load cell. S-beam load cells are named after their shape. These load cell types are made from a system of strain gauges connected to the central area in the form of a Wheatstone bridge, as shown in Figure 17 [22].

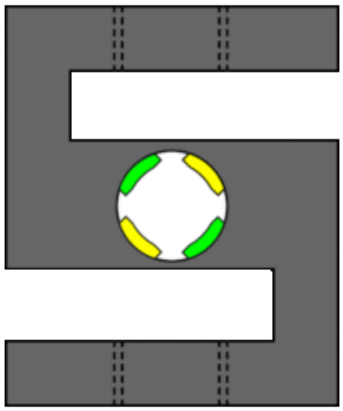

Figure 17: Structure of an S-beam load cell [22]

Strain gauges are sensors whose electrical resistance varies with changes in strain, which again is defined as the deformation or displacement of material as a result of applied stress, *i.e* the applied force to a material, divided by its cross-section. By using these principles, strain gauges convert the applied force into electrical signals which can be measured. To be able to measure these small changes in electrical resistance, the strain gauge must be connected to an electrical circuit, capable of responding to the slightest of changes. Using multiple strain gauges, connected in a divided bridge circuit, these small changes can be measured in a Wheatstone bridge.

In a Wheatstone bridge, a voltage is applied across the circuit, and the output voltage is measured across two points in the middle of the bridge, as shown in Figure 18. When unloaded, the Wheatstone bridge is balanced, and no output voltage is measured. Any impact on the strain gauge will create an imbalance which will create an output voltage to be measured. As the change in voltage is small, a signal amplifier is used, which will amplify the voltage difference, but also noise. Therefore, signal filtering has to be used in tandem with the amplification [23].

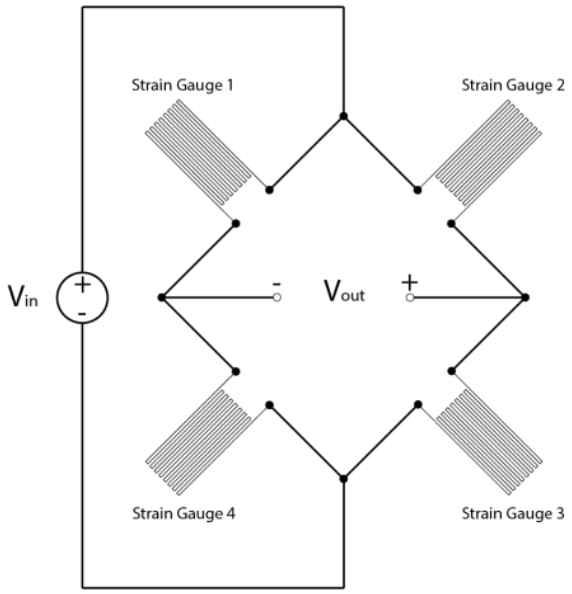

Figure 18: Wheatstone bridge [23]

Wave gauges measure the resistance of the water between two parallel rods. The resistance is proportional to the immersion depth. Using alternating current from a low impedance current amplifier, electrolysis is avoided [24].

Different software programs are used for data acquisition, data processing, and technical designs and drawings. For data acquisition, LabVIEW from National Instruments is used. LabView is a systems engineering software. In the software, virtual instruments (VIs) are created to perform the data acquisition and presentation schemes, in the form of a block diagram. The VI reads from the selected equipment, conditions the data (*i.e* applying filters), collects the data at a sampling rate of 2000 Hz, to capture the full wave, and presents the data.

For data processing, MATLAB is used. MATLAB is a programming and numeric computing platform from MathWorks. The software is used by scientists, engineers, and students for plotting and presenting data, analyzing data, creating algorithms and more [25].

Creo Parametric was used to design the plate in Figure 16. Creo is a Computer Assisted Design (CAD) software from PTC. Creo is a widely used CAD software with enough features for simple and complex designs.

The following equipment was used for the experimental setup:

- Load cell for the x-direction.
  - DBBSM-003-000, max 5 kg, Serial Number 49228.
- Load cell for the z-direction.
  - DBBSM-003-000, max capacity 5 kg, Serial Number 49227.
- Load cell for calibrating the x-direction load cell.
  - HBM U9C max capacity 200N, Serial Number 211310690
- Custom made aluminum plate presented in Figure 16.
- AluFlex profiles with varying lengths and cross sections.
- Varying bolts, washers, and nuts.
- DAQ unit, NI cDAQ-9174.
- Wave gauges, Edinburgh Designs WG8USB.
- Software LabVIEW from National Instruments.
- Software MATLAB from MathWorks.
- CAD software Creo Parametric from PTC.

4.3 Calibration Procedure

To ensure accurate and reliable measurements, the load cells need to be calibrated. According to ITTC, 10 mass increments should be used, and the full range of the load cell should be used. The load cell outputs are recorded with the applied load, and the full procedure should be done with both increasing and decreasing load increments. Lastly, the accuracy of the load cell is validated by applying miscellaneous loads of a known quantity onto the load cell, while comparing the output [26].

4.3.1 Calibration of the x-direction load cell

When calibrating a load cell placed horizontally, the load increments have to work horizontally as well. One solution is to use a pulley system and hang mass increments vertically. The drawback to this method is that the pulley will take up some of the load due to friction. Therefore, the output from the load cell will not be completely proportional to the applied mass. This could be counteracted by installing a second calibrated and accurate load cell between the pulley and the primary load cell. Then, the applied mass can be recorded by the secondary load cell, and the output of said mass is recorded by the primary load cell. This solution also has its drawbacks, as the secondary load cell could be affected if the mass increments tug hard on it when the masses are added. These proposed setups are illustrated in Figure 19.

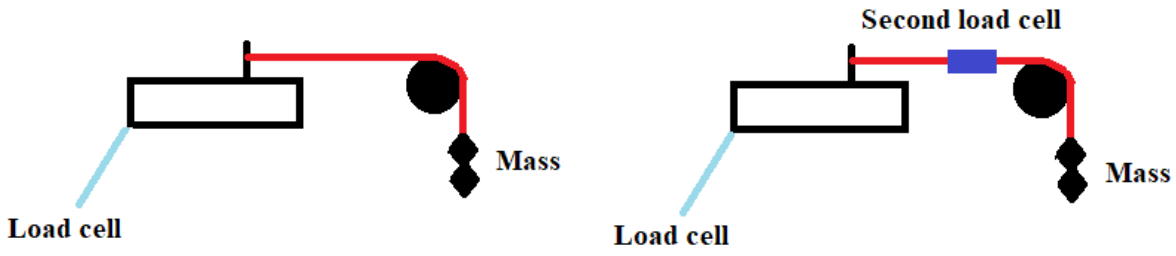

(a) Without a secondary load cell

(b) With a secondary load cell

Figure 19: Illustrations of proposed load cell calibration setup without (a), and with (b) a secondary load cell

Due to these drawbacks, another calibration setup is proposed. A threaded screw is installed between through a bracket solid, non-moving bracket with a threaded hole in the middle, and to another bracket which is allowed to slide back and forth, using locking nuts. On the movable bracket, a secondary load cell is mounted, and when the threaded screw is tightened, the load cell will pull on the primary load cell, via a spring which ensures a steady increase in load. This module was recreated after Mikkel Paulsen's master thesis "Videreutvikling av eksperimentell metode for måling av hydrodynamiske krefter på en foilseksjon" [27], and is shown in Figure 20.

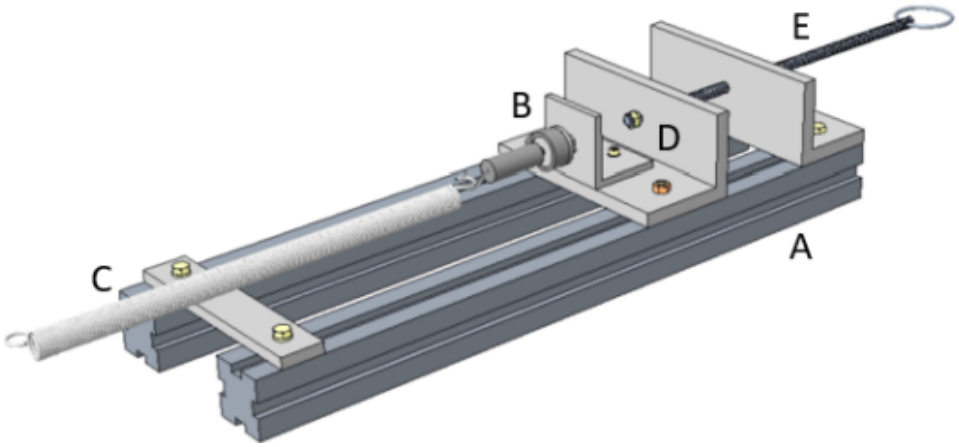

Figure 20: Calibration rig for x-direction load cell [27]

Here, A is 20x20 mm AluFlex profiles, B shows the attached secondary load cell, C is a spring installed to reduce damage potential of the load cell should jerking movement occur, D is the plate which is allowed to slide and E is the threaded rod which is tightened or loosened to adjust input force. The secondary load cell is an HBM U90 200N load cell which is deemed very accurate after calibration. The calibration of the HBM U90 200N load cell is conducted by hanging it vertically from an inflexible bar and attaching mass increments to it. The calibration steps are shown in Table 10.

Table 10: Calibration steps for HBM U9C 200N load cell

Applied load [kg]	**Load cell output [mV/V]**
0	0.005
2	-0.094
4	-0.193
6	-0.291
8	-0.390
10	-0.489
12	-0.589
14	-0.687
12	-0.589
10	-0.490
8	-0.391
6	-0.292
4	-0.193
2	-0.094
0	0.005

Using a MATLAB script provided by MarinLab, the parameters of the load cell were calculated to the presented values in Table 11.

Table 11: Load cell calibration analysis

Parameter	**Value**
Gain	-198.3 dN/d(mV/V)
Offset	1.03 N
Maximum error to linear fit	0.02 %
Maximum hysteresis	0.05 %

The gain value is programmed during measurement to properly convert the measured mV/V to N, while the offset is an adjustment to the zero point. The low maximum error to linear fit shows that the linearity between the applied and measured load behaves linearly, as desired. The low percentage of maximum hysteresis shows that the output when loading and unloading is very close to equal, as it should be. The error of full capacity and hysteresis plots are presented in Figure 21 and Figure 22.

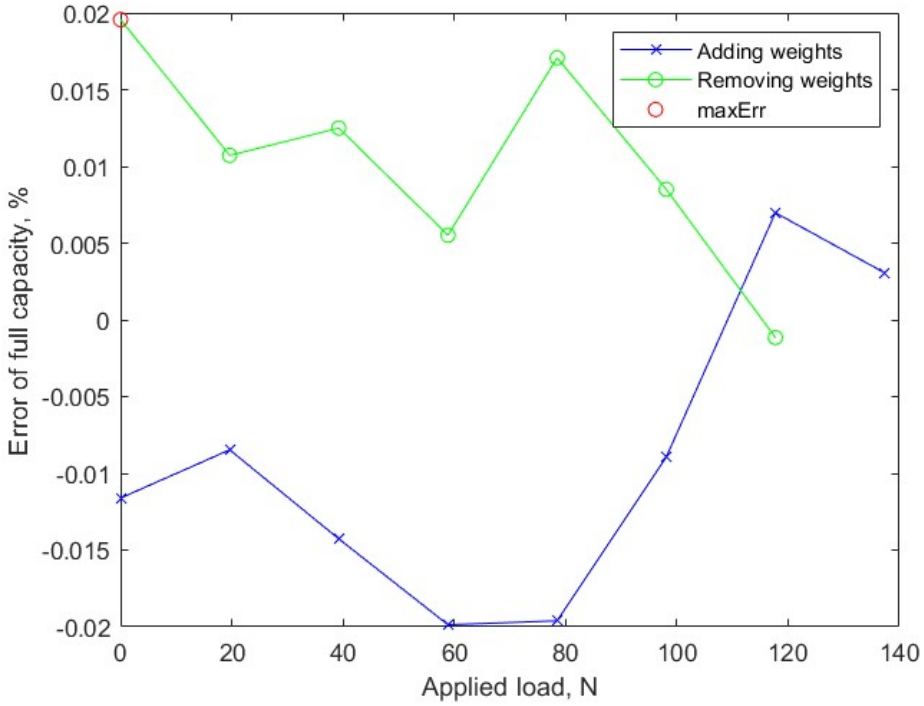

Figure 21: Maximum error of full capacity

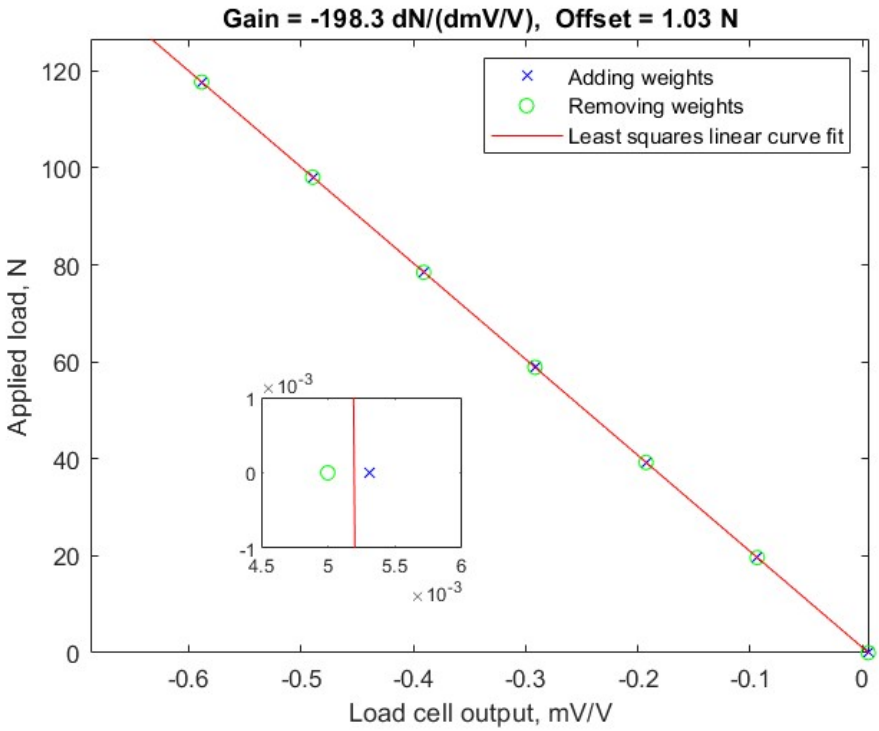

Figure 22: Hysteresis for the HBM U9C 200N load cell

As Figure 21 shows, the maximum error to linear fit occurs at 0 N applied load after unloading, which could be due to the load cell swinging after unloading, due to noise or due to not enough time allowed for the load cell to settle before recording the output.

Figure 22 shows the hysteresis. As the plot shows, the load cell works well with respect to the least squares linear curve fit. Zooming in on 0 N on the hysteresis plot, where Figure 21 showed that the maximum error occurs, the hysteresis is more visible. This is shown in the inset zoom at the hysteresis plot. Note that as the data showed, the maximum hysteresis is 0.053 %, so the scale of the x-axis in this zoom is at a magnitude of 10^{-3}.

After the calibration of the secondary HBM U90 200N load cell is complete, the calibration rig is installed on the carriage. The secondary load cell is attached through a spring, to a bolt close to where the buoy is going to be, to replicate the loading point as well as possible. The installed calibration rig, connected to the primary load cell, is shown in Figure 23.

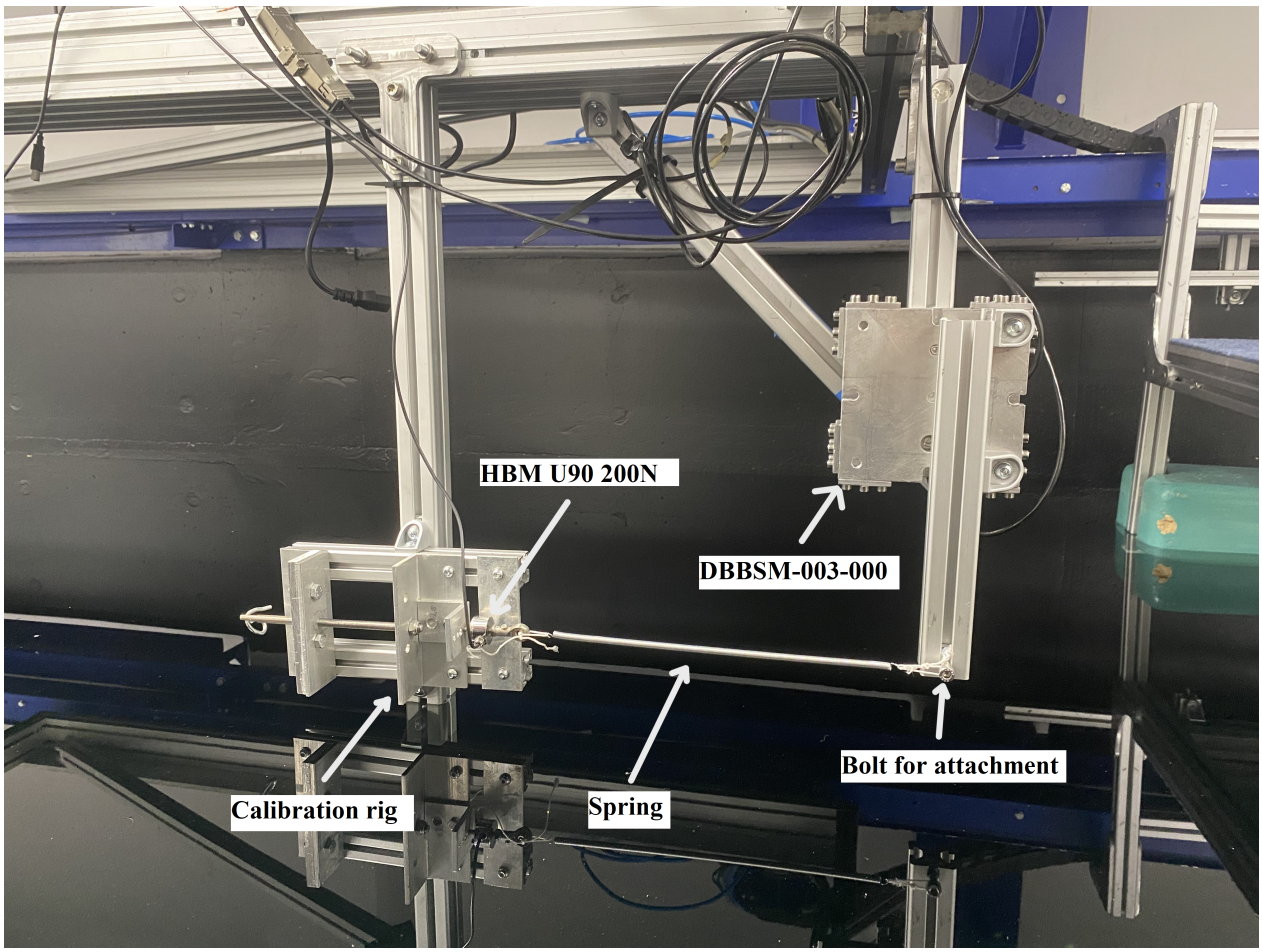

Figure 23: Image of the calibration rig connected to the x-direction load cell

By tightening the threaded rod, an evenly increasing load is applied to the primary load cell. As the applied load is measured by the HBM U90 200N load cell, the applied load is in newtons. The calibration increments are presented in Table 12.

Table 12: Calibration steps for DBBSM-003-000 load cell in x-direction. Z-direction data is included to ensure its stability during loading

Applied load [N]	**Output x-direction [mV/V]**	**Output z-direction [mV/V]**
0	-0.113	-0.660
2.11	-0.008	-0.662
5.77	0.177	-0.657
13.7	0.576	-0.653
21.8	0.984	-0.644
30.1	1.402	-0.638
38.4	1.822	-0.630
46.7	2.240	-0.626
37.5	1.776	-0.636
28.5	1.325	-0.642
19.8	0.885	-0.649
11.4	0.462	-0.658
3.45	0.062	-0.663
0.40	-0.092	-0.664
0	-0.112	-0.661

As the data shows, the output of the z-direction load cell is slightly affected by loading the x-direction load cell. The difference in the output from the z-direction load cell is only 0.038 mV/V, it should not make a major difference, but it is noted that the load cell output changes slightly in the unloaded direction.

By using MATLAB, the parameters of the load cell in the loaded direction are calculated to the values shown in Table 13.

Table 13: Load cell calibration analysis

Parameter	**Value**
Gain	19.86 dN/d(mV/V)
Offset	2.24 N
Maximum error to linear fit	0.135 %
Maximum Hysteresis	4.912 %

As with the HBM load cell, the gain is set during measurement to properly convert the measured mV/mV to N, while the offset is an adjustment to the zero point. The maximum error to linear fit is larger for the DBBSM load cell than for the HBM load cell, as expected due to the former assumption that the HBM load cell is more accurate. Still, the error to linear fit is not too high. The hysteresis is also larger for the DBBSM load cell, which could be due to the accuracy of the load cell, mistakes during the loading and unloading process, or due to the aforementioned coupling effect. The error of full capacity and hysteresis plots are presented in Figure 24 and Figure 25.

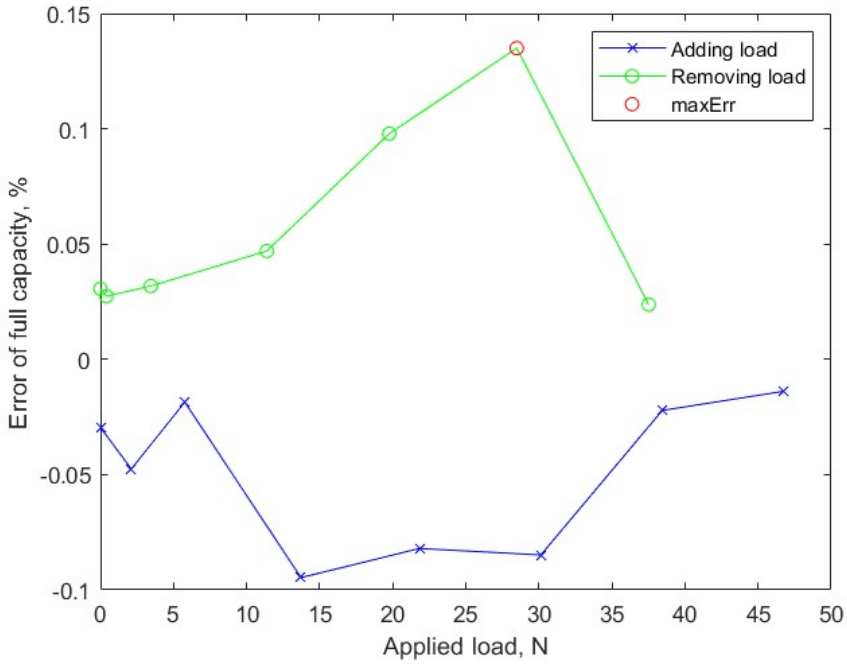

Figure 24: Maximum error of full capacity

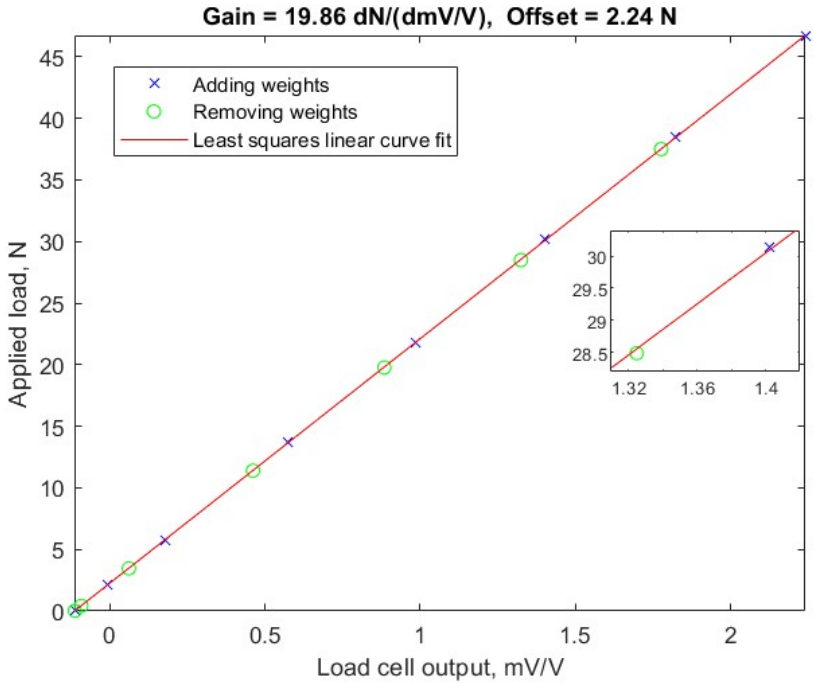

Figure 25: Hysteresis from loading and unloading the x-direction load cell

Figure 24 shows that the maximum error to linear fit occurs at approximately 30 N. Still, as Figure 25 shows, the measurements have a good correspondence to the least squares linear curve fit.

4.3.2 Calibration of the z-direction load cell

For the load cell recording the z-direction, the process is simple. A bolt with a loop is fastened to the load cell, and from the loop, the mass increments are attached. A few simplifications to the recommended ITTC recommendations are made due to limited equipment. The 10 mass increments were not possible to acquire, and the full range of the load cell was not possible to reach. Instead, 7 mass increments were used, covering a range deemed acceptable given the expected loads in the experiment itself. The outputs from both load cells are recorded to investigate possible cross-coupling effects. The mass increments and outputs recorded in this calibration procedure are presented in Table 14.

Table 14: Calibration steps for DBBSM-003-000 load cell in z-direction. X-direction data is included to ensure stability during loading

Total mass applied [kg]	**Output in x-direction [mV/V]**	**Output in z-direction [mV/V]**
0	-0.114	-0.349
0.5	-0.112	-0.565
1	-0.109	-0.780
1.5	-0.107	-0.995
2	-0.106	-1.210
2.5	-0.104	-1.426
3.5	-0.099	-1.855
4.5	-0.095	-2.283
3.5	-0.101	-1.855
2.5	-0.104	-1.425
2	-0.105	-1.210
1.5	-0.107	-0.995
1	-0.110	-0.779
0.5	-0.112	-0.563
0	-0.114	-0.348

The data shows that when loading in the z-direction, the x-direction load cell is slightly affected. As the maximum difference is 0.019 mV/V, the difference is not large, but it is noted that the load cells output changes slightly in the unloaded direction.

Further, the load cell output data in the direction to be calibrated is analyzed in MATLAB, and the following parameters in Table 15 are calculated.

Table 15: Load cell calibration analysis

Parameter	**Value**
Gain	-22.81 dN/d(mV/V)
Offset	-7.97 N
Maximum error to linear fit	0.04 %
Maximum hysteresis	-0.003 %

As with the other load cells, the gain is inserted into the data acquisition software, while the offset is used to adjust the zero point. As the load cell is connected to the x-direction load cell on one side, but free on the other side, the cross-coupling effect does not affect this load cell, unlike the x-direction load cell. This is shown by the smaller maximum error to linear fit and the low hysteresis. As stated during the calibration of the x-direction load cell, the hysteresis might be smaller due to more consideration when increasing the load increments as well. The error of full capacity and hysteresis plots are presented in Figure 26 and Figure 27.

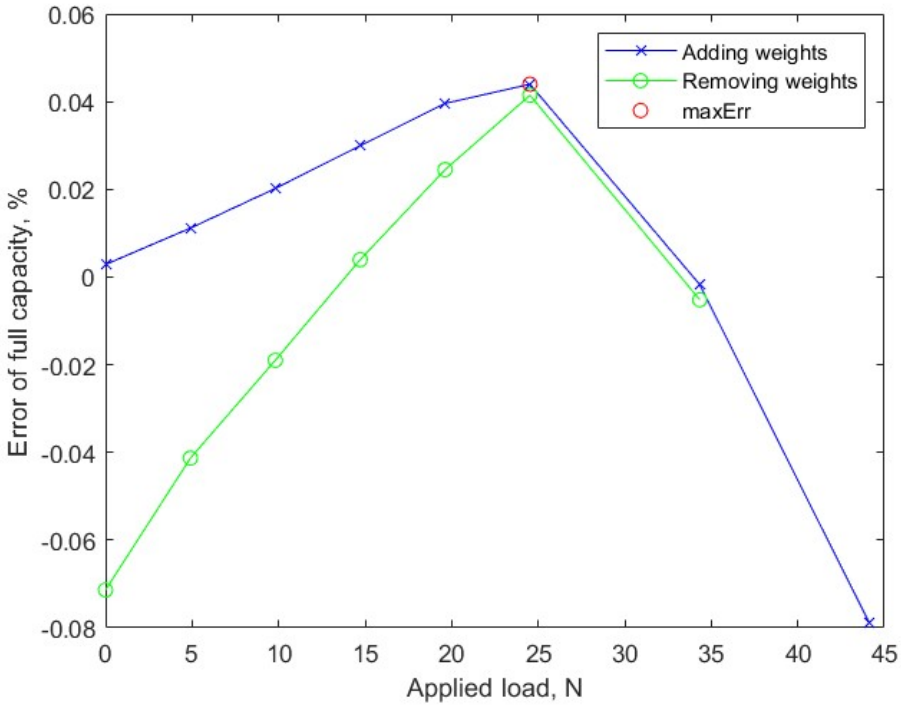

Figure 26: Maximum error of full capacity

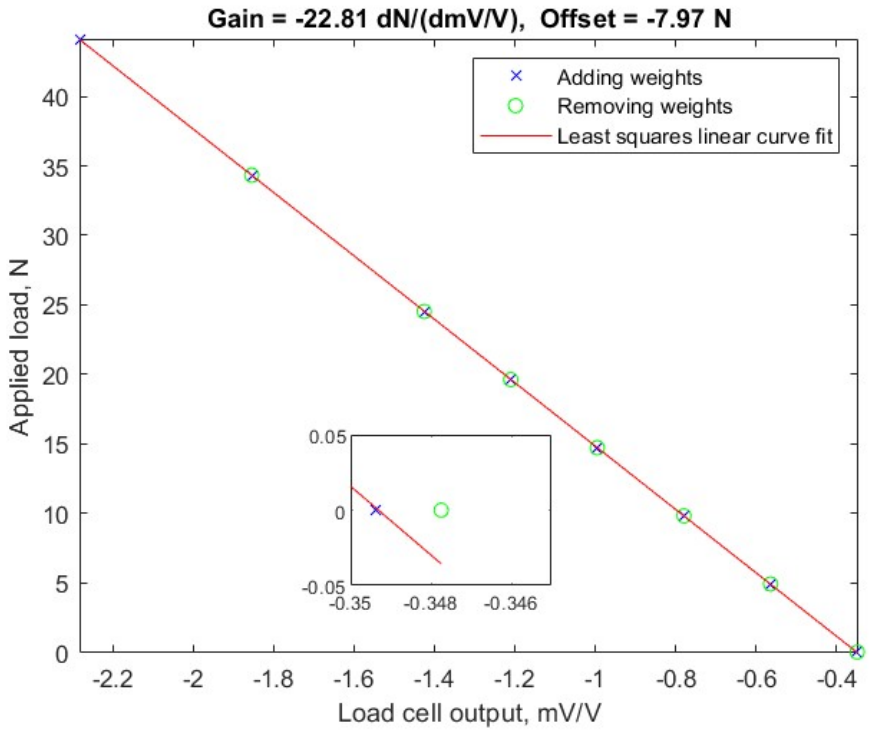

Figure 27: Hysteresis from loading and unloading the z-direction load cell

As Table 15 suggests, the linearity is intact, and the hysteresis is low. This is reflected in Figure 26, where the maximum error is low, and the curves for loading and unloading of the cell follow each other's trajectory, especially with higher loads. Figure 27 also shows that the loading and unloading process is in good correspondence with the least squares linear curve fit. The hysteresis where the maximum error to linear fit is the furthest apart, at 0 N, is zoomed in and shown in the figure. As the small range on the zoomed axes, as well as Table 15 suggests, the hysteresis is minimal.

4.4 Wave Gauge Calibration

To check whether the input data produces the desired wave, two wave gauges are installed. An attempt to record the wave data simultaneously as the loads are made by connecting a wave gauge through the same DAQ unit as the load cells. This is calibrated by checking the voltage output at the zero position (still water level), plus 10 cm and minus 10 cm from zero. Assuming linearity, the gain is calculated by solving two equations with two unknowns. Unfortunately, the attempt failed, probably due to a faulty resistor or capacitor in the recorder. While the shape of the wave and the desired simultaneity is correct, the wave height is incorrect. This is likely due to unstable gain and drift. The problem could not be solved as spare parts were not available at the facility, and even if the parts were available, the fix would be too time-consuming for the allocated time in the facility.

The other wave gauge is located beside the first one and is connected directly to the same board that controls the wave generator. To calibrate this, a program at MarinLab automatically calibrates the gain, and sets the internal resistance, by prompting the user to short-circuit the wave gauge. This is done by using a banana cable. After this procedure is carried out, a selection of waves is run through the wave generator, and the output is recorded. The waves with a frequency of 0.3 Hz are exemplified using H = 0.12 m, shown in Figure 28.

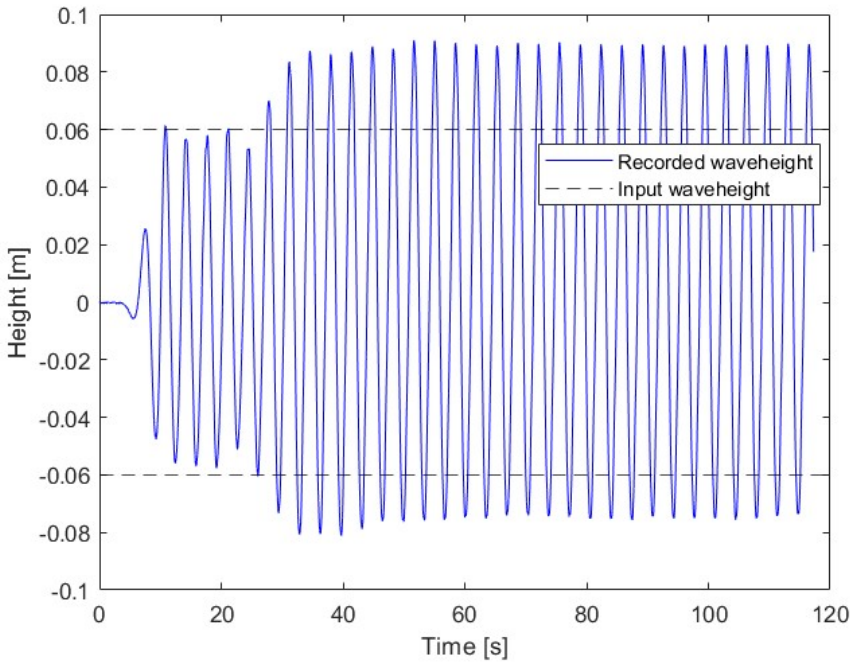

Figure 28: Recorded wave height per time for H = 0.12 m and f = 0.3 Hz

For the waves with a frequency of 0.3 Hz, an interesting phenomenon occurs. As the figure shows, after $\approx$ 20 s, the wave height increases above the input value. This is due to the wavelength corresponding to the length of the wave basin. The porous beach at the end of the tank is not able to fully absorb the energy. This causes the waves to reflect back, and due to constructive interference, standing waves are formed. To account for this, load data captured before $\approx$ 20 s will be utilized. For the other frequencies, the standing wave events do not occur, as shown in Figure 29.

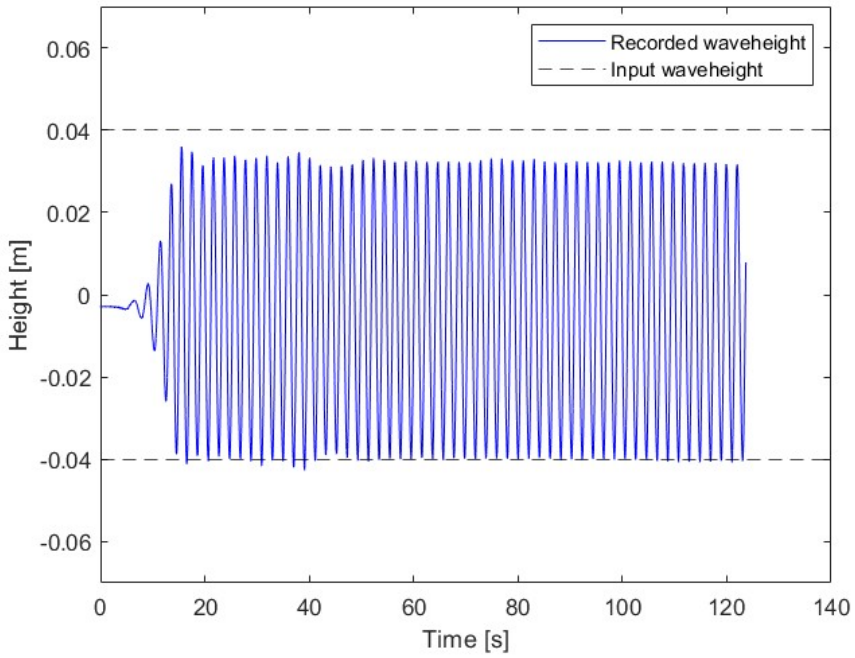

Figure 29: Recorded wave height per time for H = 0.08 m and f = 0.5 Hz

As Figure 29 shows, the wave height is close to the input for the non-standing waves. For the waves with a frequency of 0.4 Hz, the waves seem to vary between being a bit larger and smaller than the input, but within a tolerable magnitude. For the waves with a frequency of 0.5 Hz, the waves seem to be a bit smaller than the input value, especially for the waves with a wave height of 0.08 m. This wave is pushing the limit for what is acceptable, but due to time restrictions in MarinLab, it is accepted. To account for this, data captured before $\approx$ 40 s are used.

4.5 Post-Experiment Calibration

To ensure that the initial calibration of each load cell is valid, and that the gain and offset have not drifted significantly during the experiments, the load cells are re-calibrated after running the experiment. The same calibration procedure is conducted, to avoid external influence when re-calibrating. The gain, offset, maximum error to linear fit, and maximum hysteresis from the initial calibration, post-calibration, and their differences are presented in Table 16 for the x-direction load cell and Table 17 for the z-direction load cell.

Table 16: Comparison of calibration of the x-direction load cell before and after the experiment

Parameter	**Before experiment**	**After experiment**	**Difference**
Gain	19.86 dN/d(mV/V)	19.84 dN/d(mV/V)	0.02 dN/d(mV/V)
Offset	2.24 N	2.11 N	0.13 N
Maximum error to linear fit	0.14 %	0.10%	0.04 %
Maximum hysteresis	4.91 %	7.41 %	2.50 %

Table 17: Comparison of calibration of the z-direction load cell before and after the experiment

Parameter	**Before experiment**	**After experiment**	**Difference**
Gain	-22.81 dN/d(mV/V)	-22.80 dN/d(mV/V)	0.01 dN/d(mV/V)
Offset	-7.97 N	-8.09 N	- 0.12 N
Maximum error to linear fit	0.04 %	0.10 %	0.06 %
Maximum hysteresis	-0.003 %	8.816 %	8.819 %

From these tables, the load cell drift from the start to the end of the experiments looks within reason. No major shift in either gain or offset is observed. The one noticeable change is the change in maximum hysteresis in the z-direction load cell. As the load cell was calibrated by adding mass increments, the increased hysteresis may be an effect of carelessness while loading and unloading the cell. The most important factors here are still the gain and offset, to ensure that the values of the recorded data have been are reliable. As the difference in these parameters are small, compared to the ranges of loads, the data seems to be reliable.

5 Results and Discussion

This section will cover the results from 3D simulations and experimental testing. The following cases are designed to investigate the effect of wave height and frequency:

- Case 1: H = 0.08 m, f = 0.3 Hz
- Case 2: H = 0.08 m, f = 0.4 Hz
- Case 3: H = 0.08 m, f = 0.5 Hz
- Case 4: H = 0.12 m, f = 0.3 Hz
- Case 5: H = 0.12 m, f = 0.4 Hz
- Case 6: H = 0.12 m, f = 0.5 Hz
- Case 7: H = 0.16 m, f = 0.3 Hz
- Case 8: H = 0.16 m, f = 0.4 Hz
- Case 9: H = 0.16 m, f = 0.5 Hz
- Case 10: H = 0.04 m, f = 0.5 Hz
- Case 11: H = 0.20 m, f = 0.5 Hz
- Case 12: H = 0.24 m, f = 0.5 Hz
- Case 13: H = 0.12 m, f = 0.6 Hz
- Case 14: H = 0.12 m, f = 0.7 Hz

Here, H and f are wave height and frequency, respectively.

5.1 3D Simulation Results

This subsection will cover the data processing procedure and the resulting plots from the 3D simulations.

Figure 30 shows an example of a simulated wave. The numerical 3D simulated data is zeroed to only account for effects from the waves, the initial data from before the solution stabilizes is cut out, and the magnitude of the data points is doubled, due to the symmetry boundary condition.

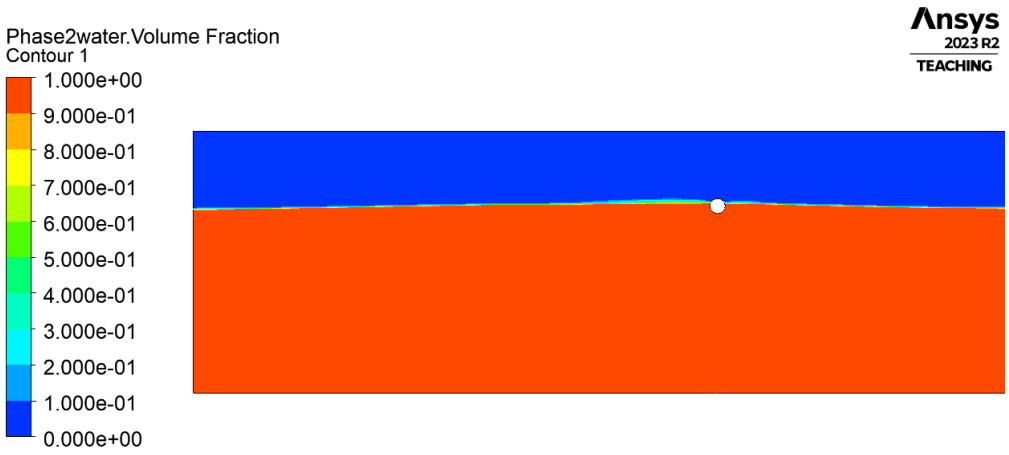

Figure 30: Simulated wave moving along the fluid domain

For all cases, the data is cut after the solution stabilizes. This is shown in Figure 31 and Figure 32 as an example, of lift and drag forces, respectively.

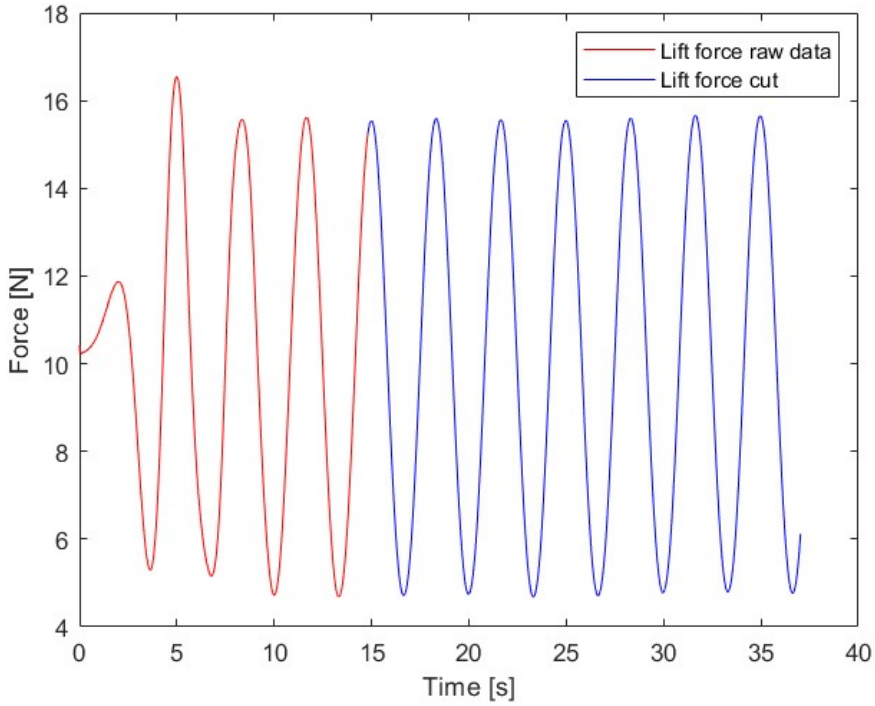

Figure 31: Raw and cut lift force data for Case 1

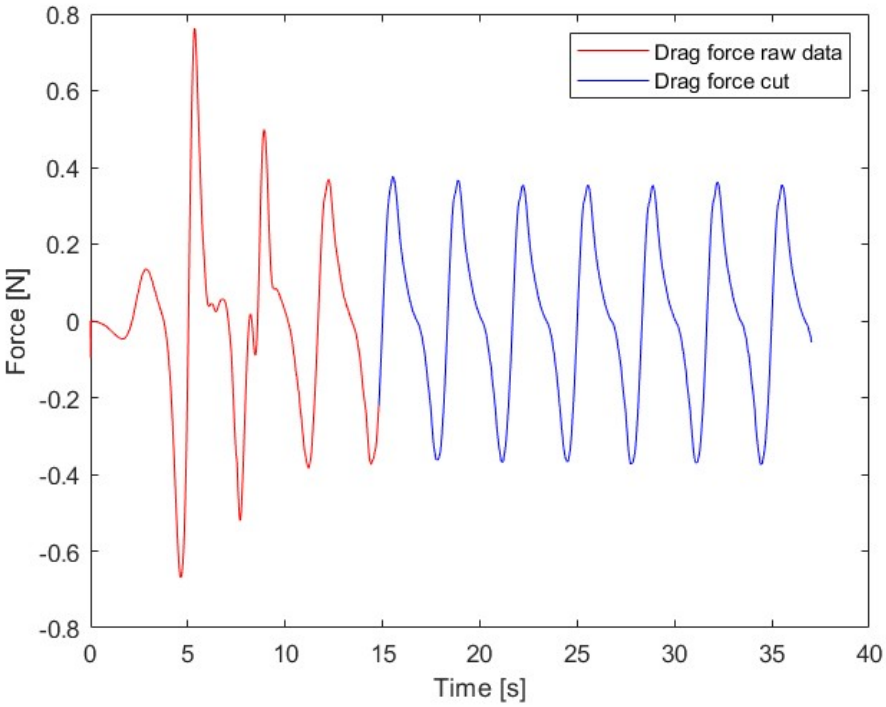

Figure 32: Raw and cut drag force data for Case 1

As the figures show, the data stabilizes a bit before the data is cut, but a safety margin is used to ensure only stable data is considered. The plot also shows that the oscillations are offset from zero. Therefore, the mean value of the cut data is calculated, and subtracted from the data points. In addition, as the symmetry attribute is used, this force is only for half the sphere, and therefore, the data points are doubled to account for symmetry. An example of zeroed and doubled forces plot for Case 5 is shown in Figure 33. Where the lift forces oscillate harmonically between their crests and troughs, the drag forces have a plateau where the force is zero, when the lift forces are at their lowest. This is likely due to the momentary halt in motion as the waves go from a descending to an ascending motion when the vertical direction gradient is equal to 0. The drag force is at its maximum when the lift force is descending from its apex, as that is the moment the most mass passes, respective to the horizontal x-direction.

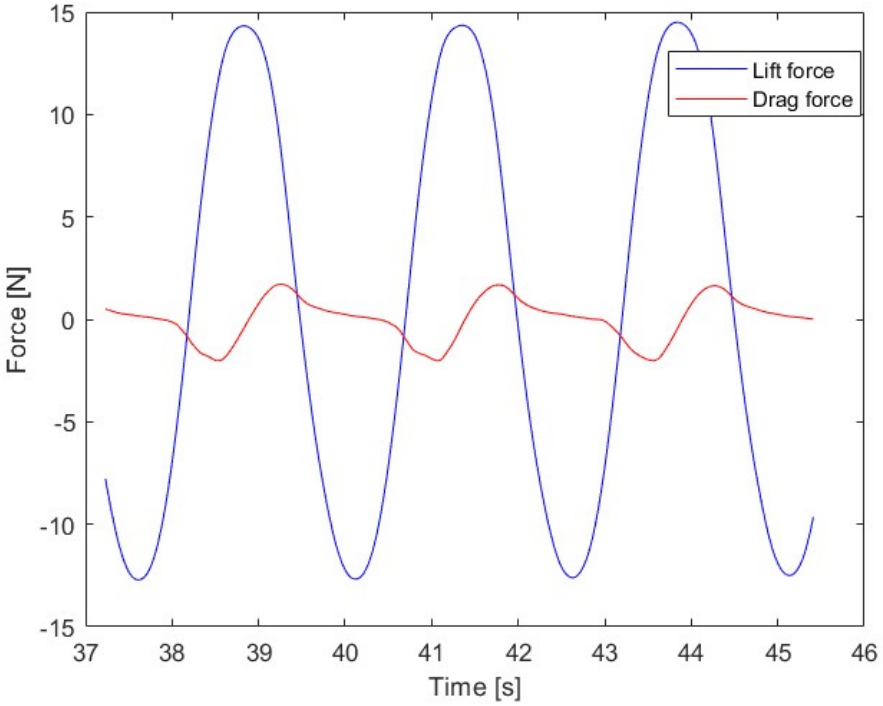

Figure 33: Drag and lift force for Case 5 after zeroing and doubling

5.2 Experimental Testing Results

For the experimental tests, the data was collected for a duration of 10 s. As shown in section 4.4, the data is captured before the standing wave phenomena occur for waves with a frequency of 0.3 Hz. For the rest of the waves, a later duration can be used, to allow maximum time for the waves to build up. As the LabVIEW software is used to zero the data after the sphere is mounted and submerged, and before the waves are generated, the output can be directly plotted in MATLAB, without cutting or zeroing. As the force patterns are the same for all cases, the plot for Case 5 is shown in Figure 34 as an example. The lift force oscillates harmoniously around zero, while the drag force has a plateau when the lift force is at its maximum. Unlike the 3D simulated plots, the zero-force plateau appears when the lift force is at its highest. This is because the x-direction load cell was calibrated against the wave motion direction, and therefore, it appears phase-shifted compared to the simulated data. The same hypothesis for the plateauing phenomena in the 3D simulated plots is valid here.

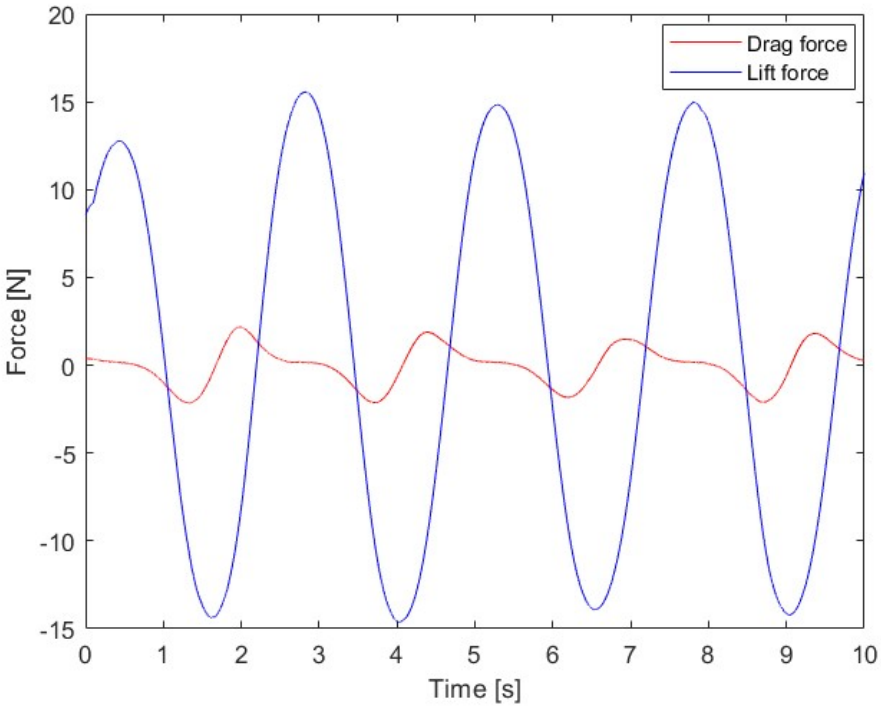

Figure 34: Experimental drag and lift force for Case 5

5.3 Comparing Numerical and Experimental Forces

After extracting the data from the simulations and the experimental tests, the data can be compared to analyze the accuracy of the numerical method. To better show the differences, the drag and lift forces will be shown separately, and the simulated data will be shifted to the experimental data to make the peaks and bottoms overlap. The comparative plots are shown in Figure 35 for the drag force and Figure 36 for the lift force.

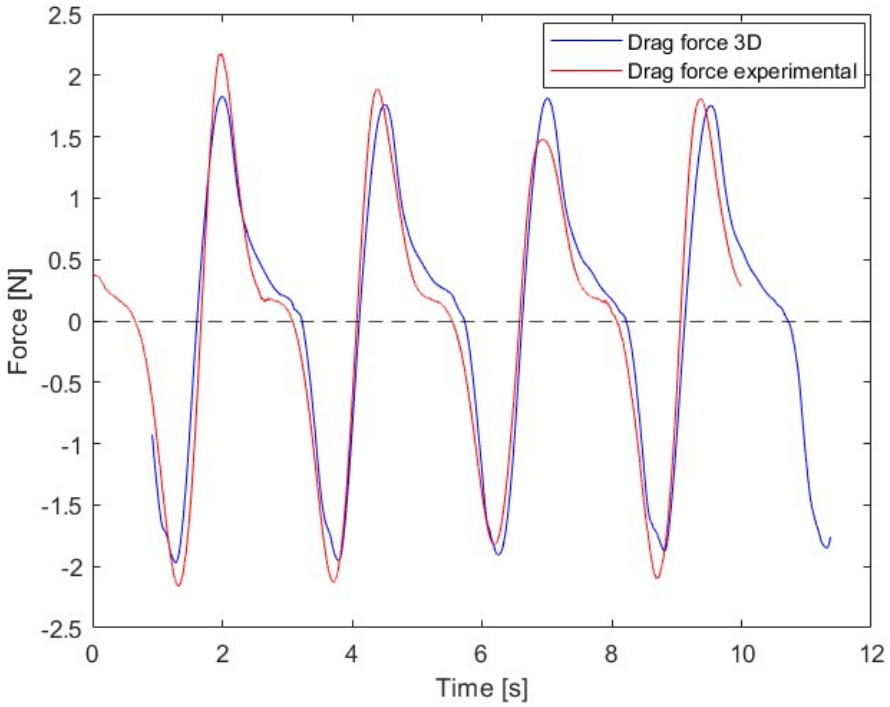

Figure 35: Comparison of simulated and experimentally recorded drag force data for Case 5

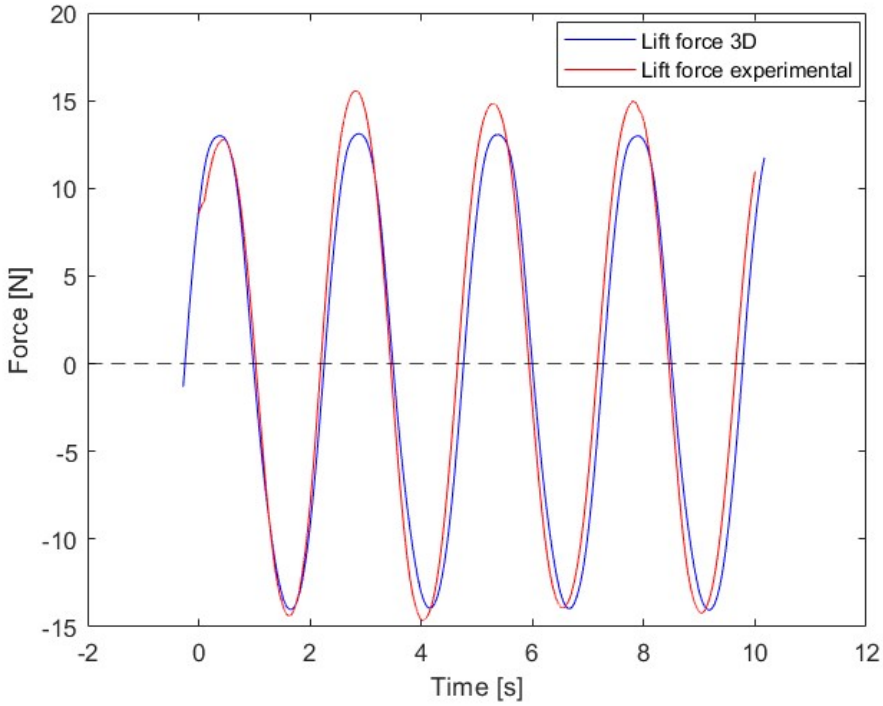

Figure 36: Comparison of simulated and experimentally recorded lift force data for Case 5

These plots show that the drag and lift forces follow the same pattern for both numerical and experimental data. The larger waves seem to have a slight difference between numerical and experimental data, which will be analyzed later.

The average of the maximum and minimum drag force and lift force from 3D and experimental tests are shown for each case in Table 18 and Table 19, respectively. The maximum and minimum forces are calculated by reading the force values of every crest and trough for 3D and experimental data for each case and taking the average force value of said wave crests and troughs. Cases 10 to 14 are simulated after the experimental tests were conducted, so only numerical data is available. Figure 37 and Figure 38 show the effect of increasing wave height on the induced drag and lift forces for cases with the same frequency.

Table 18: Maximum and minimum drag force for each case

Case	**3D simulation [max/min]**	**Experimental results [max/min]**
1	0.8 N/-0.7 N	0.7 N/-0.7 N
2	1.1 N/-1.1 N	1.0 N/-1.1 N
3	1.7 N/-1.6 N	1.5 N/-1.5 N
4	1.2 N/-1.3 N	1.2 N/-1.2 N
5	1.9 N/-1.9 N	1.9 N/-2.1 N
6	3.0 N/-3.0 N	3.0 N/-2.8 N
7	1.9 N/-1.7 N	2.0 N/-1.8 N
8	3.0 N/-3.0 N	3.1 N/-3.1 N
9	4.1 N/-4.6 N	4.6 N/-4.3 N
10	0.7 N/-0.7 N	-
11	5.6 N/-5.8 N	-
12	6.2 N/-6.8 N	-
13	4.7 N/-4.4 N	-
14	5.4 N/-5.3 N	-

Table 19: Maximum and minimum lift force for each case

Case	**3D simulation [max/min]**	**Experimental results [max/min]**
1	10.8 N/-10.9 N	10.7 N/-10.4 N
2	10.5 N/-10.6 N	10.2 N/-10.2 N
3	10.2 N/-9.8 N	10.0 N/-9.6 N
4	14.7 N/-13.8 N	14.9 N/-14.9 N
5	13.3 N/-13.9 N	14.6 N/-14.3 N
6	12.9 N/-12.4 N	14.2 N/-13.3 N
7	18.5 N/-15.0 N	18.5 N/-18.0 N
8	16.8 N/-15.5 N	18.5 N/-17.0 N
9	15.0 N/-15.1 N	17.1 N/-15.9 N
10	5.2 N/-5.4 N	-
11	15.9 N/-16.2 N	-
12	18.3 N/-17.8 N	-
13	11.4 N/-11.7 N	-
14	10.1 N/-10.8 N	-

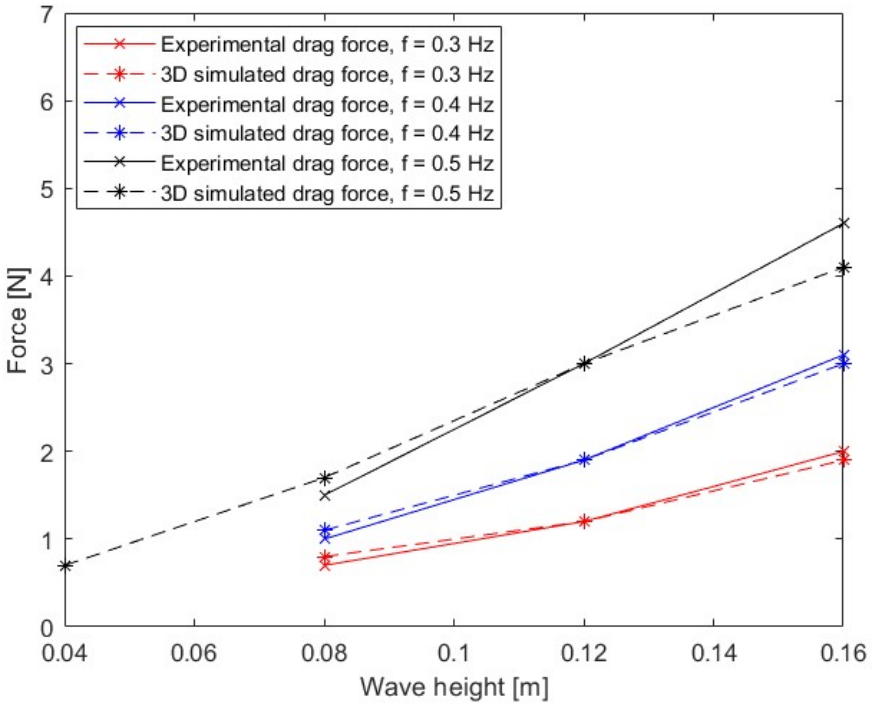

Figure 37: Effect of increasing wave height at constant frequency for drag forces

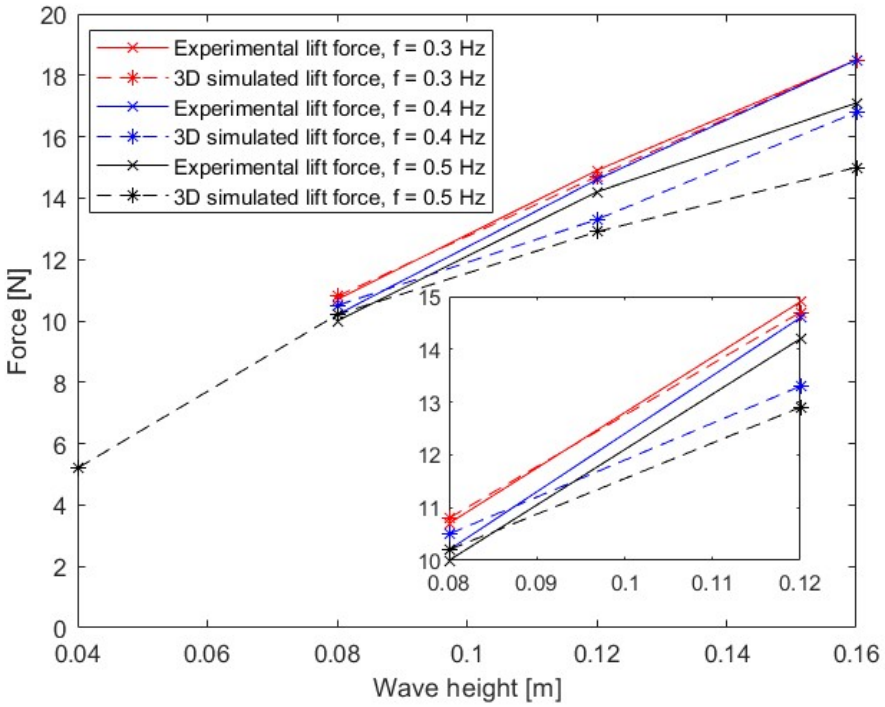

Figure 38: Effect of increasing wave height at constant frequency for lift forces

These charts show that the drag and lift force increases with increasing wave height. A larger wave height means that the amount of mass transported both horizontally and vertically increases, leading to larger forces. The simulated and experimental drag forces are in good agreement for all wave heights. This difference between experimental testing and numerical simulations could be due to a lot of factors. While the resolution of the mesh around the sphere was increased, it could still be insufficient for the slight difference in amplitudes. The difference could also come from the wave theory applied to solve the governing equations or from the numerical interpretation of how the fluid interacts with the sphere surface.

As for the lift force, Figure 38 shows that for larger wave heights, there is a difference between the simulated and experimental lift forces. However, for larger wave heights, the lift force diverges between simulated and experimental results. This can be because of the fact that the highest wave is close to the radius of the sphere, and the waves go over the sphere (as shown in Figure 39), which could reduce the lift force by loading from the top. During experimental testing, this is not observed, and it can be due to the structural connection at the top of the sphere.

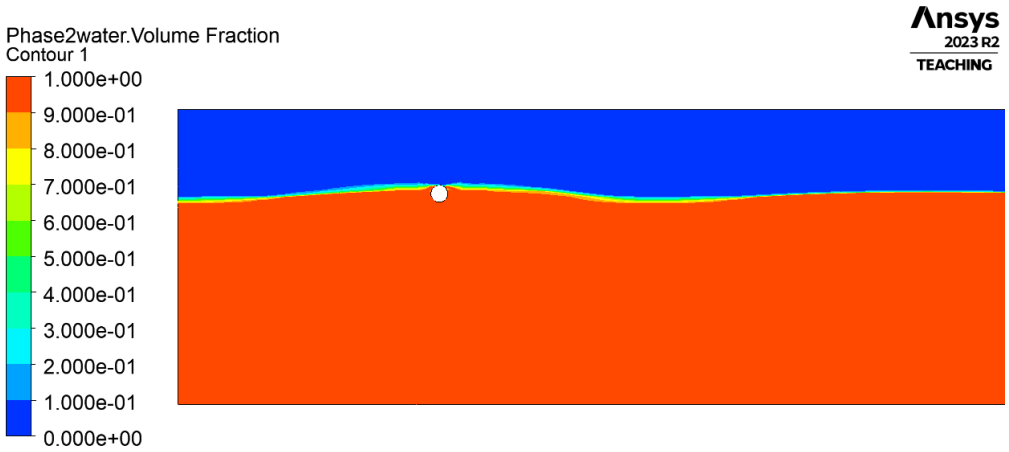

Figure 39: Wave going over the sphere at maximum wave height

The effect of the wave frequency is investigated for the cases with the same wave height, as shown in Figure 40 for the drag force and Figure 41 for the lift force.

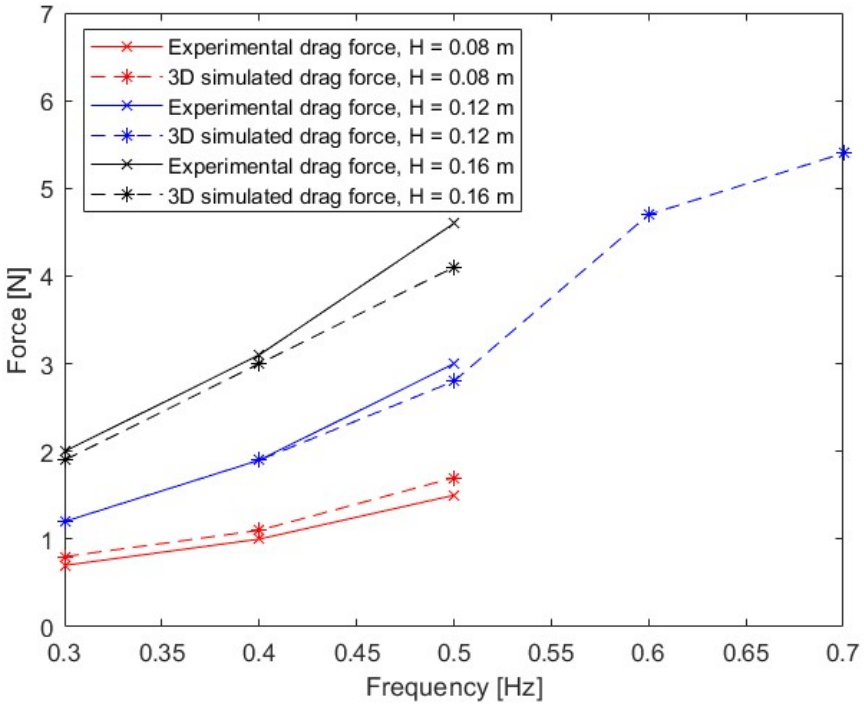

Figure 40: Effect of increasing frequency at constant wave height for drag forces

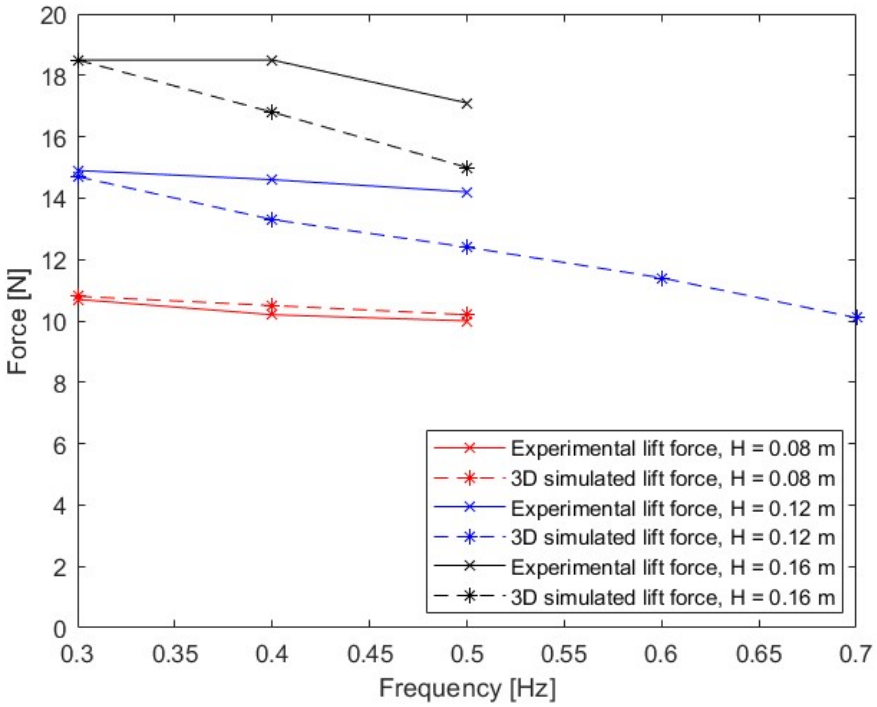

Figure 41: Effect of increasing frequency at constant wave height for lift forces

These figures show a direct relation between the forces and the frequency. The drag force is shown to increase and the lift force is shown to decrease when the frequency is increased. The charts also show that the numerically simulated forces and the experimentally measured forces diverge when the frequency increases, especially for H = 0.12 m and H = 0.16 m. This could be due to the fact that an increase in frequency is in direct relation to a decrease in period. This means that the time between incoming waves decreases, which could lead to interactions between subsequent waves. Interactions between waves could explain this observed trend, as horizontally, the waves could be strengthened, while vertically, an incoming ascending wave could be partially canceled by a former, descending wave.

5.4 Energy Calculations

This subsection will cover the available energy in the different wave cases, the harvestable energy, and the energy related to the experimentally measured loads.

5.4.1 Theoretically calculated available energy in the waves

The available energy in the waves is calculated using the total energy formulation given in Equation 28. The variables in the equation are density ρ, which is assumed to be constant at 998.2 kg/m^3, the gravitational acceleration g, assumed to be 9.81 m/s^2, the wave amplitude ζ_A, which varies between cases and the wavelength λ, which also varies from case to case. In addition, as this equation calculates the available energy per unit at width (y-direction), the resulting energy is multiplied by 0.2 (diameter of the sphere) to calculate the available energy in the channel leading to the sphere. The results are presented in Table 20.

Table 20: Available wave energy for the different cases

Case	Frequency [Hz]	Wave amplitude [m]	Wavelength [m]	Energy [J]
1	0.3	0.04	14.0	21.9
2	0.4	0.04	9.2	14.4
3	0.5	0.04	6.2	9.7
4	0.3	0.06	14.0	49.4
5	0.4	0.06	9.2	32.4
6	0.5	0.06	6.2	21.9
7	0.3	0.08	14.0	87.7
8	0.4	0.08	9.2	57.7
9	0.5	0.08	6.2	38.9

As the table shows, the available energy decreases with increasing frequency. This is due to the available energy being dependent on the wavelength, and an increasing frequency yields a decreasing wavelength, as the dispersion relation shown in Equation 16 is proportional with the period, which in turn is inversely proportional with the frequency. At the same time, the available energy is dependent on the wave height squared, and as such, increases with wave height.

5.4.2 Energy available for harvesting

As MarinLab is not equipped to measure energy, the simulated cases with good agreement with experimental results will be considered for the calculation of harvestable energy. The cases included here are the cases for which the wave height is 0.08 m and the frequency is 0.3 Hz, *i.e.* cases 1, 2, 3, 4, and 7.

To analyze the energy harvestable by the sphere, the parameters from section 2.2.6 need to be calculated. Here, the coefficients and forces are extracted from the simulations per time step. The forces, coefficients, and cap areas for one full wave cycle are shown in Figure 42 for the drag direction and Figure 43 for lift direction, using Case 1 as an example. With these parameters, Equation 40 is used to calculate the velocity variation during one period of the wave. For Case 1, this is shown in Figure 44.

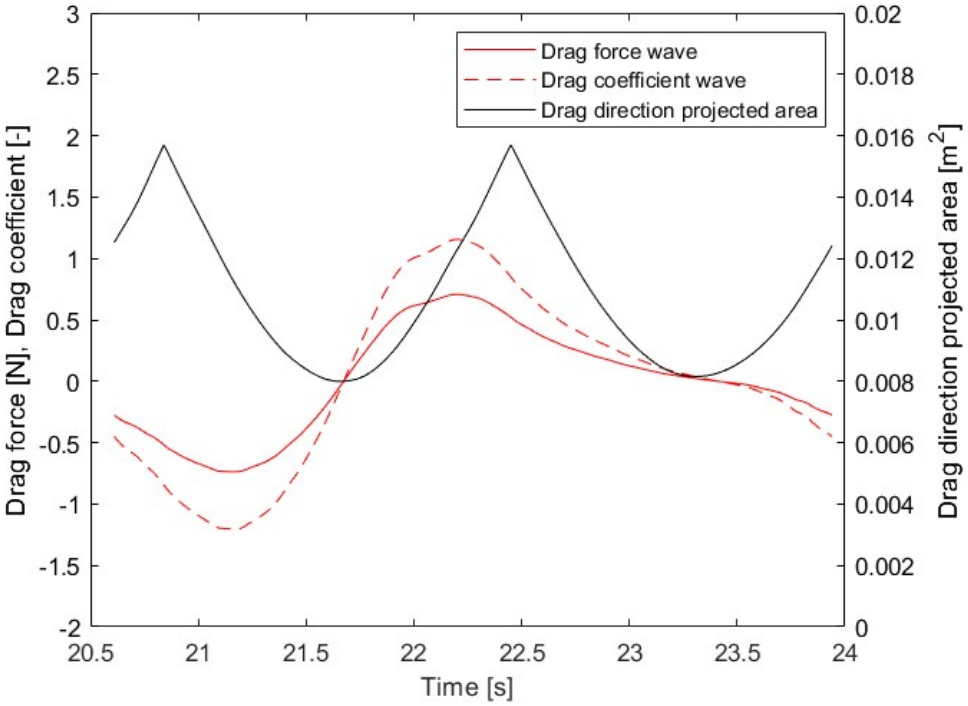

Figure 42: Drag direction parameters for one wave cycle

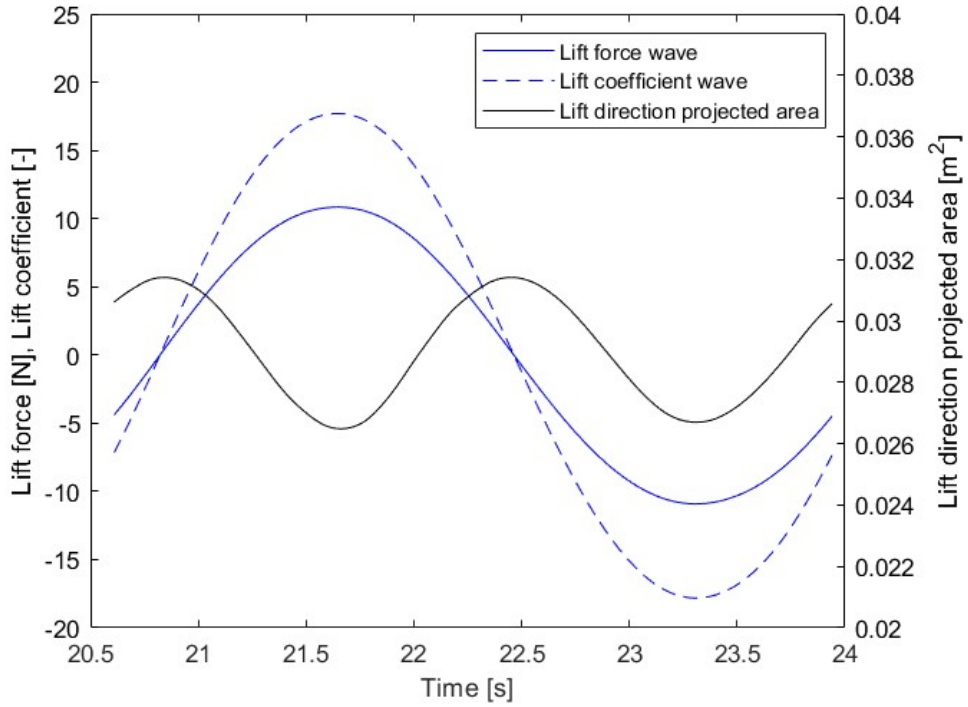

Figure 43: Lift direction parameters for one wave cycle

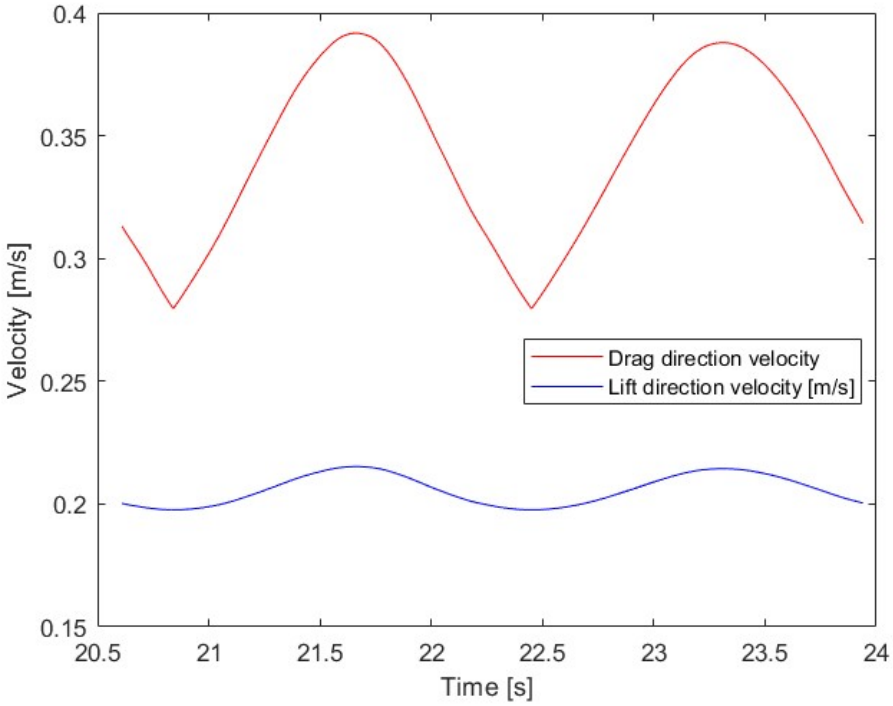

Figure 44: Drag and lift direction velocity for one wave cycle

Following, the absolute value of the velocity is multiplied with the absolute value of the force recorded at each time step, over the full wave cycle. The absolute values are used as the focus is to analyze the magnitude of energy. This yields the wave power for each time step as Equation 29 shows. The harvestable wave power in the drag and lift directions during a full wave cycle is shown in Figure 45. The power is numerically integrated over a wave period T, as shown in Equation 30, to calculate the energy for a full wave cycle. The resulting energy in drag and lift direction, as well as the total energy calculated by taking the sum of the energies, are shown in Figure 46.

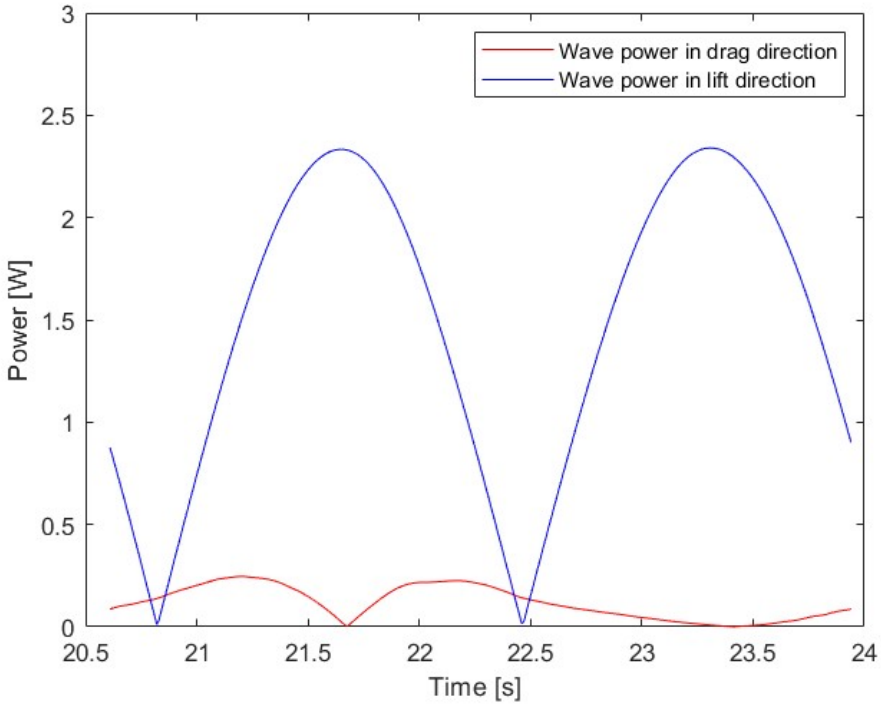

Figure 45: Wave power in drag and lift directions for one wave cycle

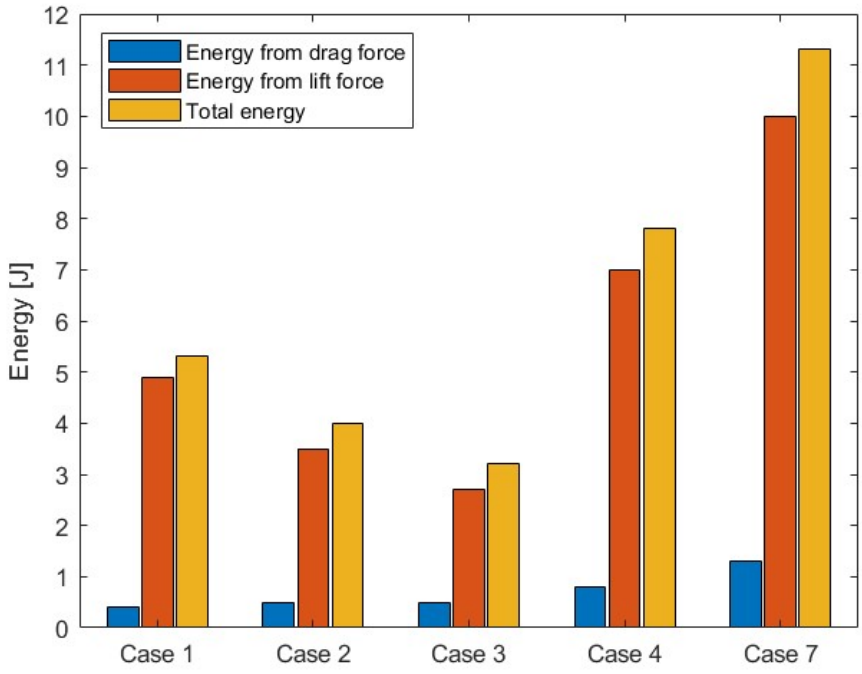

Figure 46: Energy from the drag and lift forces, and the total energy

As the chart shows, the total energy is sourced by the energy from the lift forces. The energy that can be harvested increases with increasing wave height, while it decreases with increasing frequency. As cases 1, 2, and 3 have the same wave height of 0.08 m, there is a clear decrease in the energy from lift forces, while there can be observed a slight increase in energy from drag forces. This corresponds with the trends seen from the force analysis. In total, this leads to a decrease in energy. When looking at cases 1, 4, and 7, which all have the same frequency of 0.3 Hz, with increasing wave heights, the energy available for harvesting from both drag and lift forces increases significantly. As a larger wave height implies a larger mass transport, this is expected.

5.4.3 Comparing theoretically available energy with harvestable energy

To determine the usefulness of a spherical object for wave energy conversion, the percentage of the harvestable energy over the available energy is used. This is shown in Figure 47.

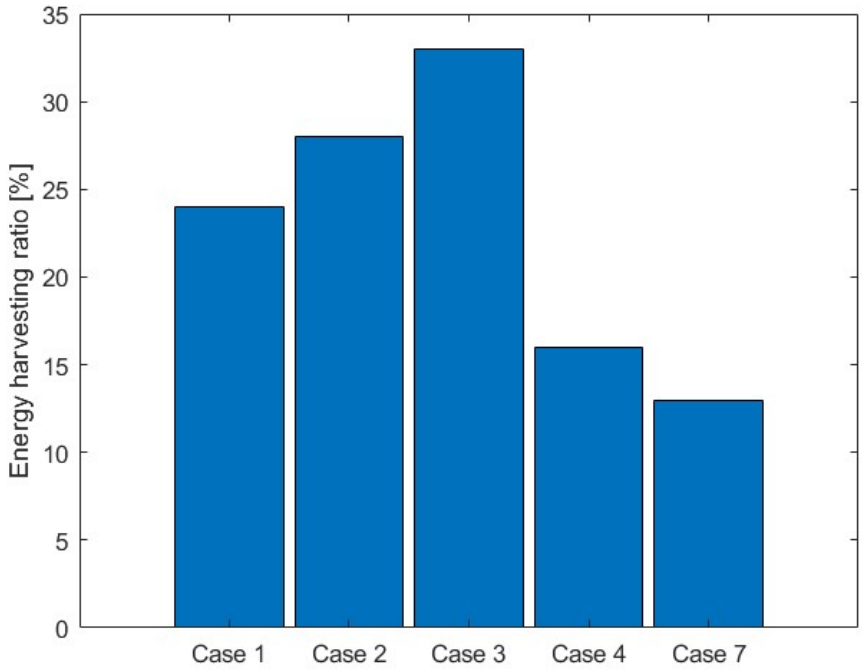

Figure 47: Energy harvesting ratio of a spherical object for the different wave cases

Figure 46 shows that the harvestable energy increases and decreases proportionally to increasing H and f, respectively. Figure 47, on the other hand, shows that the energy harvesting ratio increases when f increases and decreases when H increases. This could be due to the fact that as the wave height increases, the water surface interacts with a smaller projected diameter

and area. A larger wave height leads to a higher amount of energy absorbed by the sphere, as it is in direct relation with an increase in mass transport, while the energy harvesting ratio decreases. The increase in the energy harvesting ratio observed with increasing frequency could have a similar explanation. Increasing the frequency does not change the projected area the wave surface interacts with, while an increased frequency is proportional to a decrease in the theoretically calculated available energy.

As an increasing frequency yields both a higher energy ratio and an increased amount of waves passing the sphere per unit time, a half-submerged spherical wave energy converter could function better in areas with shorter and more frequent waves. As a spherical object absorbs a smaller fraction of higher waves carrying more energy, it could mean that this shape is not ideal for wave energy conversion. However, this could be advantageous in scenarios where potentially damaging waves are formed, *i.e.* during storms.

6 Conclusion

This thesis aims to contribute to further research on the optimization of wave energy converters. The parameters that have been researched are wave loads onto a spherical object, the energy corresponding to these loads, the available energy in waves, and the percentage of available energy absorbed by the sphere. As wave energy could contribute to the energy mix as a stable source, this thesis has aimed to contribute to developing this field.

6.1 Key Findings

The thesis found that both drag and lift forces onto the object increased with increasing wave height, as an increase in wave height implies an increase in mass transport onto the object. Increasing frequencies, on the other hand, lead to an increase in drag force, and a decrease in lift force onto the object. It is theorized that these effects are due to the effects of waves interacting with each other around the sphere, as an increase in frequency is equivalent to a shorter period, and hence, shorter time between the incoming waves. In the horizontal direction, it could mean that not all of the mass being transported has the time to pass by the sphere, with subsequent incoming waves forcing this extra mass across the sphere. In the vertical direction, the shorter time between waves could lead to an incoming wave being partially canceled out by the remainder of the previous wave descending after interacting with the sphere.

Further, the available energy and energy absorbed by the sphere was calculated. The available energy increased with increasing wave height and decreased with increasing frequency. This is due to the equation used to calculate the available energy, Equation 28, being proportional to the wave amplitude squared, and to the wavelength, which is proportional to the wave period, which is inversely proportional to the frequency. This pattern was reflected by the total energy absorbed, which increased with increasing wave height and decreased with increasing frequency. The total energy was defined as the sum of energy parallel to the drag force and lift force. The energy from drag and lift force followed the same patterns as the forces. Both energies increased with increasing wave height, while the energy from drag force increased and the energy from lift force decreased with increasing frequency. As these energy definitions were proportional to their respective forces, this is expected.

When looking at the ratio of energy absorbed by the sphere to the available energy in the wave, *i.e.* the energy harvesting ratio, shown in Figure 47, this ratio decreased with increasing wave height. The leading theory is that, as the majority of the energy in a wave is at the surface, the increase in wave height also leads to the surface interacting with a smaller projected area, especially as the sphere is in a fixed position. Thus, the increase in available energy from increasing wave height leads to more energy absorbed by the sphere, but a lesser share of the total available energy.

6.2 Contribution to the Current Research

As the field of wave energy has a large potential, but is a largely untapped source of energy, this thesis has contributed to further optimizing wave energy converters and creating a baseline for the maximum percentage of available energy that can be harvested from a half-submersed, fixed, spherical wave energy converter.

6.3 Further Work

To build on this thesis, it would be interesting to see how the energy harvesting ratio changes with different submersion ratios. As the energy harvesting ratio in this thesis declined for increasing wave heights, and as it is theorized that this is due to the wave interacting with a reduced projected area, it would be interesting to analyze how this ratio could change with different submersion levels, especially for a fully submersed sphere. For lower submersion levels than half submersion, there would probably be a similar reduction in the projected area for smaller waves. While a fully submersed sphere would probably not get the same impact from the wavefront, it could stabilize the harvesting ratio for a larger variety of waves, as all of the fluid would pass over it.

It would also be interesting to test a spherical object's ability to absorb waves from an irregular sea state, both in simulations and in an experimental testing facility. The wave paddles in MarinLab can create JONSWAP, Bretschneider, and Pierson-Moskowitz spectra, and other facilities might be able to create other spectra. This could contribute to researching spherical wave energy converters, by testing the effects of a more realistic sea state.

On the experimental setup, there is more research that can be carried out. As mentioned in the Experimental Method section, the load cells could interact with each other, reducing the reliability of the data. A study of different load cell setups, and optimizing the entire experimental setup, would make the laboratory testing more reliable, strengthening further development. Jacob Andersen and Morten Bech Kramer [28] have conducted research into different setups, where a system of six pretensioned wires with one degree of freedom force transducers was found to be the most accurate for a fixed sphere, more than a six-degree of freedom load cell setup mounted at the top of the sphere. Further testing of which setups could be assembled at MarinLab could not only improve research on wave energy, but all research performed using load cells at the facility.

Further, replacing the fixed setup with a floating object, and investigating mooring options, would contribute to wave energy converter technology, especially in deep waters, where bottom-fixed mounting is not feasible.

References

[1] Global energy review: Co2 emissions in 2021. Technical report, IEA paris, 2022.

[2] T-Z. Ang, M. Salem, M. Kamarol, H.S. Das, M.A. Nazari, and N. Prabaharan. A comprehensive study of renewable energy sources: Classifications, challenges and suggestions. *Energy Strategy Reviews*, 43:100939, 2022.

[3] B. Drew, A.R. Plummer, and M.N. Sahinkaya. A review of wave energy converter technology. *Proceedings of the Institution of Mechanical Engineers, Part A: Journal of Power and Energy*, 223(8):887–902, 2009.

[4] A.B.S. Bahaj. Generating electricity from the oceans. *Renewable and Sustainable Energy Reviews*, 2011.

[5] A. Clément, P. McCullen, A. Falcão, A. Fiorentino, F. Gardner, K. Hammarlund, G. Lemonis, T. Lewis, K. Nielsen, S. Petroncini, M-T. Pontes, P. Schild, B-O. Sjöström, H.C. Sørensen, and T. Thorpe. Wave energy in europe: current status and perspectives. *Renewable and Sustainable Energy Reviews*, 6(5):405–431, 2002.

[6] T.W. Thorpe et al. A brief review of wave energy. 1999.

[7] R. Pelc and R.M. Fujita. Renewable energy from the ocean. *Marine Policy*, 26(6):471–479, 2002.

[8] S. Foteinis. Wave energy converters in low energy seas: Current state and opportunities. *Renewable and Sustainable Energy Reviews*, 162:112448, 2022.

[9] G.K. Batchelor. *An Introduction to Fluid Dynamics*. Cambridge University Press: Cambridge, England, 1967.

[10] B.E. Launder and D.B. Spalding. *Lectures in Mathematical Models of Turbulence*. Academic Press, London, England, 1972.

[11] D.C. Wilcox. *Turbulence Modelling for CFD, Third Edition*. DCW Industries, Inc., 2006.

[12] F.R. Menter. Zonal two equation k-ω turbulence models for aerodynamic flows. *AIAA Paper 93-2906*, 1993.

[13] J.E. Welch, F.H. Harlow, J.P. Shannon, and B.J. Daly. The mac method-a computing technique for solving viscous, incompressible, transient fluid-flow problems involving free surfaces.

[14] C.W. Hirt and B.D. Nichols. Volume of fluid (vof) method for the dynamics of free boundaries. *Journal of Computational Physics*, 39(1):201–225, 1981.

[15] ©ANSYS, Inc. *ANSYS User Manual Release 12.0*, 2009.

[16] Shyam2791 - own work. https://commons.wikimedia.org/w/index.php?curid=22702507.

[17] J. Králik. Cfd simulation of air flow over an object with gable roof, revised with y+ approach. Vysoká škola báňská-Technická univerzita Ostrava, 2016.

[18] G. Russo L. Pareschi. *Implicit–Explicit Runge–Kutta schemes for stiff systems of differential equations*, volume 3, pages 269–288. 01 2001.

[19] B. Pettersen. *Marin Teknikk 3 Hydrodynamikk*. Akademika, 2022.

[20] O. Bühler. *Waves and Mean Flows*. Cambridge University Press, The Edinburgh Building, Cambridge CB2 8RU, UK, 2009.

[21] Department of Mechanical and Marine Engineering. Marinlab. Technical report, Høgskulen på Vestlandet.

[22] Applied Measurements Ltd. Load cells and force sensors. https://appmeas.co.uk/products/load-cells-force-sensors/, 18.09.2023.

[23] Michigan Scientific Corporation. What is a strain gauge? https://www.michsci.com/what-is-a-strain-gauge/, 18.09.2023.

[24] E-design Ltd. Wave gauges. http://www4.edesign.co.uk/product/wavegauges/, 19.09.2023.

[25] MathWorks. Matlab. https://se.mathworks.com/products/matlab.html, 2023.

[26] *ITTC - Recommended procedures and guidelines 7.6-02-09*, 2002. Work instructions, Calibration of load cells.

[27] M. Paulsen. Videreutvikling av eksperimentell metode for måling av hydrodynamiske krefter på en foilseksjon, Universitetet i Bergen, 2022.

[28] J. Andersen and M.B. Kramer. Wave excitation tests on a fixed sphere: Comparison of physical wave basin setups. In *Proceedings of the European Wave and Tidal Energy Conference*, volume 15, 2023.